Bayesian Geoacoustic Inversion of Seabed Reflection Data at the New England Mud Patch

by

Josée Belcourt
B.Eng., Royal Military College of Canada, 2011

A Thesis Submitted in Partial Fulfillment of the
Requirements for the Degree of

MASTER OF SCIENCE

in the School of Earth and Ocean Sciences

Bayesian Geoacoustic Inversion of Seabed Reflection Data at the New England Mud Patch

by

Josée Belcourt
B.Eng., Royal Military College of Canada, 2011

Supervisory Committee

Dr. Stan E. Dosso, Supervisor
School of Earth and Ocean Sciences

Dr. N. Ross Chapman, Member
School of Earth and Ocean Sciences

Dr. Jan Dettmer, Member
School of Earth and Ocean Sciences

Supervisory Committee

Dr. Stan E. Dosso, Supervisor
School of Earth and Ocean Sciences

Dr. N. Ross Chapman, Member
School of Earth and Ocean Sciences

Dr. Jan Dettmer, Member
School of Earth and Ocean Sciences

Abstract

This thesis presents Bayesian geoacoustic inversion of seabed reflection-coefficient data as part of the U.S. Office of Naval Research Seabed Characterization Experiment 2017 at the New England Mud Patch. First, a linearized, ray-based Bayesian inversion of acoustic arrival times is carried out for high-precision estimation of experiment geometry and uncertainties, representing an important first step to inferring seabed properties using geoacoustic inversion methods such as reflection inversion. The high-precision estimates for source-receiver ranges, source depths, receiver depths, and water depths at reflection points along the survey track are used to calculate grazing angles, with angle uncertainties computed using Monte Carlo methods. The experiment geometry uncertainties are obtained using analytic linearized estimates, and verified with nonlinear analysis. Second, a trans-dimensional (trans-D) Bayesian inversion of reflection-coefficient data is carried out for geoacoustic parameters and uncertainties of fine-grained/cohesive sediments. The trans-D inversion samples probabilistically over an unknown number of seabed interfaces and the parameters of a zeroth- or first-order autoregressive error model. The numerical method of parallel tempering reversible jump Markov-chain Monte Carlo sampling is employed. Spherical-wave reflection coefficient modelling is applied using plane-wave decomposition in the Sommerfeld integral. The inversion provides marginal posterior probability profiles for Buckingham's viscous grain-shearing parameters: porosity, grain-to-grain compressional modulus, material exponent, and compressional viscoelastic time constant as a function of depth in the sediment. These parameters are used to compute dispersion relationships for each layer in the model, providing marginal posterior probability profiles for compressional-wave velocity and attenuation at different frequencies, as well as density. The geoacoustic inversion results are compared to independent mea-

surements of sediment properties.

Table of Contents

List of Tables

List of Figures

Acknowledgements

I would like to thank my supervisor and teacher Stan Dosso for significantly increasing the likelihood of my success with his prior knowledge and immense support throughout my degree; my co-author Jan Dettmer for providing the code and technical support that made this thesis possible; my co-author Charles W. Holland for the measured data presented in this work, quality assurance at every step, and for being an excellent host during my visit to the Applied Research Laboratory at Penn State University; and the U.S. Office of Naval Research and the Canadian Department of National Defence for financially supporting this work.

Dedication

To my fiancé, Bradley J. Spencer, who's name I will take shortly.

Far better an approximate answer to the right question,
which is often vague,
than an exact answer to the wrong question,
which can always be made precise.

John W. Tukey, 1962

Chapter 1

Introduction

Sound propagation in shallow water is strongly influenced by interaction with the seabed. The study of bottom-interacting sound is an active area of underwater acoustic research for shallow-water areas, namely the continental terrace (shelf and slope), are of great geotechnical, economic, and military importance. Yet, knowledge of seabed geoacoustic parameters (e.g., sound velocity, density, and attenuation) often represents the limiting factor in modelling ocean bottom-interacting acoustic fields [1, 2]. Recently, the geoacoustic properties of soft, muddy seabeds have become of interest to shallow-water acoustic research as they are commonly found on the continental terrace [2–4], but have been studied less and are poorly understood compared to harder seabeds such as sands [5, 6].

The inversion of acoustic data provides a non-intrusive and economical alternative to direct measurements (e.g., coring) for estimating seabed parameters. For example, seabed reflection coefficients, measured as a function of grazing angle and frequency, provide an informative data set for inferring the geoacoustic parameters of a layered seabed model, and geoacoustic inversion of reflection-coefficient data has received wide attention over the years, e.g., [7–12]. However, inferring geoacoustic parameters (in general) requires solving an inherently nonunique, nonlinear inverse problem, and rigorous estimates of data and model uncertainties are required, e.g., [13–16].

Two of the main objectives of the U.S. Office of Naval Research (ONR) Seabed Characterization Experiment 2017 (SCBEX) at the New England Mud Patch are to quantify uncertainties in seabed parameters estimated by geoacoustic inversion and assess the resulting geoacoustic models and inversion methods [17]. Accordingly, this work presents trans-dimensional (trans-D) Bayesian inversion of reflection-coefficient data from two sites at the New England Mud Patch, providing geoacoustic parameter estimates and uncertainties for fine-grained/cohesive (muddy) sediments as part of

SCBEX.

The New England Mud Patch is a ∼13,000 km^2 area roughly 100 km south of Cape Cod, MA, characterized by fine-grained sediments, including clay- and slit-sized particles, over a strong reflecting layer composed of coarse-grained (sandy) sediments [18–20]. In this work, reflection-coefficient data were collected at the Shallow Water Acoustic Measurement Instrument (SWAMI) and Piston Core 52 (PC52) sites within the New England Mud Patch area. The measurement geometry involved a broadband source towed near the surface of the water, and two omni-directional receivers moored far enough above the seabed to prevent interference between direct- and bottom-reflected acoustic paths. The reflection-coefficient data are computed from time-windowed acoustic arrivals and corrected for various experimental effects (source directivity, geometric spreading, and absorption) [21, 22]. To do so, accurate knowledge of the experiment geometry is required. Hence, the first part of this thesis develops a linearized, ray-based Bayesian inversion of acoustic arrival time data for high-precision experiment geometry and uncertainties. The second part of this work presents the trans-D Bayesian geoacoustic inversion of seabed reflection coefficients for fine-grained/cohesive sediments.

In general, an inverse problem uses observed data to estimate (infer) parameters of a postulated model that characterizes a physical system [23]. Conversely, a forward problem computes (predicts) data that would be observed in an experiment given a model of the physical system. The inverse problem cannot be solved without being able to first solve the forward problem. Here, the observations are high-resolution seabed reflection coefficients and the physical system (seabed) is described by the physics of Buckingham's viscous grain-shearing (VGS) theory [24–26] which considers unconsolidated sediments as a viscous fluid containing sediments grains in contact. The theory predicts frequency dependence similar to Biot's theory [27] at low to intermediate frequencies, although the physics of dispersion differ. According to Biot theory, dispersion in poroelastic media is caused by fluid viscosity only, whereas VGS theory considers both fluid viscosity and friction (grain-to-grain shearing).

The estimated parameters (from VGS theory) consists of a set of depth-dependent parameters (i.e., vary from layer to layer), and another set of parameters which are taken to be layer/depth independent (i.e., a single value for all sediment layers) [10,28]. The depth-dependent parameters include porosity, grain-to-grain compressional modulus, material exponent, and compressional viscoelastic time constant. The depth-independent parameters include interstitial fluid density and bulk modulus, and granular density and modulus. In this work, the forward problem predicts spherical-wave

(full-wave) reflection coefficients because the common plane-wave approximation is not sufficient when measurements include sub-bottom waves that arrive at multiple angles different from the specular [11, 21, 29]. Computationally, spherical-wave reflection coefficients are predicted using plane-wave decomposition in the Sommerfeld integral [10, 11].

The Bayesian approach to inverse problems assumes the model is not deterministic but a random variable to be described statistically (probabilistically) [23]. The method samples the posterior probability density (PPD), incorporating both data and prior information. The solution can be quantified in terms of properties of the PPD representing model parameter estimates and uncertainties which are computed using numerical methods for highly nonlinear inverse problems.

The choice of model parametrization (e.g., number of seabed interfaces) is nontrivial and strongly influences parameter uncertainty estimates. Trans-D inversion is a general and powerful approach to Bayesian model selection in geoacoustic inverse problems for depth-dependent seabed models [30–32]. The trans-D formulation incorporates the number of parameters (e.g., number of seabed interfaces and parameters of a zeroth- or first-order autoregressive data error model) as an unknown in the problem. The trans-D PPD intrinsically addresses model selection and accounts for parameter uncertainty due to model parametrization by integrating over possible parametrization choices [33, 34]. This thesis explores trans-D Bayesian inversion based on a parallel tempering reversible-jump Markov-chain Monte Carlo (rjMCMC) sampling method [33–37]. The method is applied to measured reflection-coefficient data to estimate the geoacoustic parameters of a depth-dependent seabed model of an unknown number of interfaces.

The body of this thesis contains two chapters which correspond to two papers on Bayesian inversion associated with SCBEX at the New England Mud Patch. As these articles were produced as stand-alone works, there is some repetition across the chapters in the introductory material, experiment geometry, and theory. The following provides a brief overview of this work.

Chapter 2 (to be submitted as [38]) presents a linearized Bayesian approach to inverting acoustic arrival-time data for high-precision estimation of experiment geometry and uncertainties. The source-receiver ranges, source depths, receiver depths, and water depths at reflection points along the track are estimated to much higher precision than prior information based on GPS and bathymetry measurements. The high-precision experiment geometry is used to calculate seabed reflection (grazing) angles, with angle uncertainties computed using Monte Carlo methods. The experi-

ment geometry uncertainties, obtained using analytic linearized estimates, are verified with nonlinear analysis.

Chapter 3 (to be submitted as [39]) presents the trans-D Bayesian geoacoustic inversion. The inversion is applied to high-resolution broadband reflection-coefficient data from two sites of contrasting mud-layer thicknesses. Trans-D inversion, sampling over an unknown number of seabed interfaces and the parameters of a zeroth- or first-order autoregressive error model, and spherical-wave reflection coefficient modelling are employed. The inversion provides parameter estimates with uncertainties quantified in terms of marginal posterior probability profiles for VGS model parameters. The VGS parameters are used to compute dispersion relationships for each layer in the model to yield compressional-wave velocity and attenuation as functions of frequency, as well as density as a function of layer. Results of the acoustic inversion are compared to independent measurements of sediment properties collected at the experiment sites.

Chapter 4 gives a brief summary and discussion of the work presented in this thesis.

Chapter 2

Linearized Bayesian Inversion for Experiment Geometry at the New England Mud Patch

This chapter presents a linearized Bayesian approach to inverting acoustic arrival-time data for high-precision estimation of experiment geometry and uncertainties associated with geoacoustic inversions as part of the U.S. Office of Naval Research (ONR) Seabed Characterization Experiment 2017 (SCBEX) at the New England Mud Patch. The data were collected at the Shallow Water Acoustic Measurement Instrument (SWAMI) site using an impulsive ship-towed source and two moored omni-directional receivers for the purpose of carrying out broadband reflectivity inversion, a geoacoustic inversion method that requires accurate knowledge of the survey geometry. To provide this, a Bayesian ray-based inversion is developed here that estimates source-receiver ranges, source depths, receiver depths, and water depths at reflection points along the track to much higher precision than prior information based on GPS and bathymetry measurements. Near the closest point of approach, where rays are near vertical, data information is low and inaccurate range estimates are improved using priors from analytic predictions based on nearby sections of the track. Uncertainties are obtained using analytic linearized estimates, and verified with nonlinear analysis. The high-precision experiment geometry is subsequently used to calculate grazing angles, with angle uncertainties computed using Monte Carlo methods.

The measured data presented here were collected at sea by Charles W. Holland. Stan Dosso provided an initial MATLAB code for array element localization which was substantially adapted by the author of this thesis for the purpose of this work. Moreover, the author picked arrival times for direct, bottom-reflected, and bottom-

surface-reflected acoustic paths as data for the linearized inversions, carried out the inversions, and wrote the paper on which this chapter is based.

2.1 Introduction

The inversion of acoustic arrival-time data for high-precision estimation of experiment geometry and uncertainties is an important first step to inferring seabed properties using geoacoustic inversion methods such as broadband, wide-angle reflection inversion [9, 21, 22, 40]. Quantifying uncertainties in seabed parameters estimated by geoacoustic inversion and assessing the resulting geoacoustic models and inversion methods are two of the main objectives of SBCEX at the New England Mud Patch, a major collaborative study funded by ONR [17]. The initial step of high-precision estimation of experiment geometry is key as sufficiently-accurate source and receiver locations are often not known after deployment at sea and precise experiment geometry is required to calculate reflection coefficients used to infer the geoacoustic properties of the seabed. While this chapter presents a new high-precision inversion to estimate experiment geometry for the purpose of reflection-coefficient inversion (carried out in Chapter 3), many other applications in geoacoustic inversion and advanced signal processing also require accurate knowledge of experiment geometry.

Although the data considered here were collected for acoustic reflection-coefficient inversion, the survey design lends itself to using the arrival times for high-precision estimation of experiment geometry without the need for a separate localization survey. The acoustic measurements involved a broadband source mounted to a catamaran equipped with GPS towed behind a ship with signals recorded at two bottom-moored omni-directional receivers. The source emitted a short acoustic pulse every second along a $\sim$1.6-km (20-minute) radial track designed to pass close to directly above the receivers, with the track roughly centered on the closest point of approach (CPA) to the receivers. Arrivals of interest include the direct, bottom-reflected, and bottom-surface-reflected paths. The survey is described in greater detail in Section 2.2.

To further motivate the high-precision estimation of experiment geometry, Fig. 2.1 shows range and direct arrival-time differences between the source/receiver geometry based on GPS measurements taken during the experiment and the geometry estimated in the acoustic inversion carried out in this chapter. Fig. 2.1(a) shows an average range difference of 4.7 m with variability of $\sim$1 m (upper curve) due to errors/variability in source and receiver GPS locations. In comparison to these range differences, the lower curve of Fig. 2.1(a) shows the inversion range uncertainties which are about 0.2–0.3 m

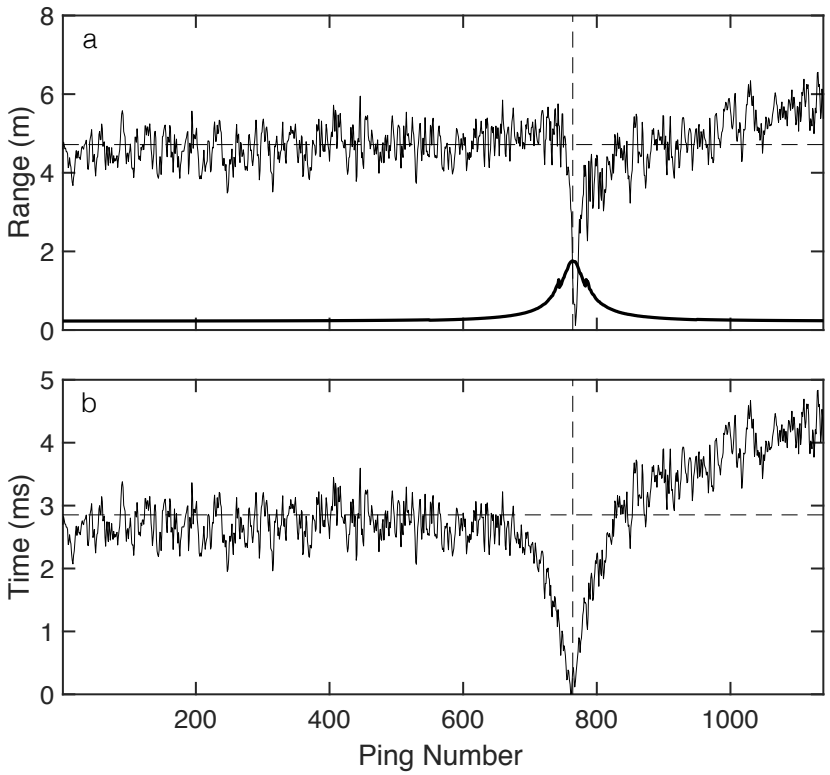

Figure 2.1: Range and direct-arrival time differences between GPS measurements during the survey and acoustic inversion results estimated here. (a) shows the source-receiver range differences between GPS and inversion as a function of source transmissions (referred to as pings) (upper curve) and inversion range uncertainties (lower curve). (b) shows differences between direct-path arrival times computed for the GPS source and receiver locations and the locations estimated by acoustic inversion. The horizontal and vertical dashed lines indicate mean values and CPA, respectively.

over most of the track but increase to about 1.8 m near CPA. The figure highlights the significant reduction in uncertainty achieved by inverting acoustic arrival-time data. Fig. 2.1(b) shows that the direct arrival-time differences are about 3 ms over most of the track, with a variability of about 1 ms. To compute the time differences in Fig. 2.1(b), the GPS range information was converted to direct-arrival estimates using ray tracing and compared to the measured direct arrivals. Using an average sound speed of 1473 m/s, the mean time difference of 3 ms equates to a range difference of 4.2 m, which is roughly consistent with the mean range difference of 4.7 m observed in Fig. 2.1(a).

The high-precision experiment geometry estimation carried out here uses a linearized, ray-based Bayesian inversion algorithm [41–43]. The Bayesian inversion addresses significant sources of error in the experiment, and incorporates physical prior

information about the solution in addition to the measured data. The acoustic data include arrival times of direct-path signals over the entire track, and bottom-reflected and bottom-surface-reflected arrivals out to moderate ranges where these arrivals could be clearly identified. The unknown geometric parameters considered in the inversion include source-receiver ranges, source depths, water depths for the bottom-reflected paths, receiver depths, and receiver synchronization corrections. In addition to the data, the Bayesian inversion applies Gaussian prior densities based on GPS and bathymetry measurements. A track estimation algorithm [44] is used to augment range priors near CPA where the data poorly constrain the solution. The inversion results are subsequently used to compute reflection (grazing) angles at the seabed, as required to calculate reflection coefficients for geoacoustic inversion.

The experiment geometry uncertainties are estimated efficiently from the linearized approximation of the posterior covariance matrix and compared to uncertainties obtained by a nonlinear Monte Carlo [23] approach based on calculating error statistics from an ensemble of noisy synthetic inversion results. The grazing angle uncertainties are also estimated by a similar Monte Carlo appraisal. The Monte Carlo method is computationally intensive but represents a fully nonlinear solution which can be used to confirm results obtained by linearized approximation.

The remainder of this paper is organized as follows: Section 2.2 describes the experiment and data collection process. Section 2.3 presents the theory and implementation of the ray-tracing algorithm (Section 2.3.1), develops the linearized Bayesian inversion and uncertainty estimation (Section 2.3.2), presents the track prediction approach to augmenting the range prior near CPA (Section 2.3.3), and explains the computation of grazing angles and uncertainties (Section 2.3.4). The inversion results are presented in Section 2.4. Section 2.5 describes the nonlinear uncertainty estimation carried out to validate the linearized inversion. Finally, Section 2.6 summarizes and discusses this work.

2.2 Experiment

The SCBEX experiment site is located approximately 110 km south of Cape Cod, MA, and characterized by a smooth, flat seabed with predominantly silt-sized particles. The acoustic data presented in this chapter were collected at the SWAMI site on March 31, 2017, at 40.4614°N, −70.5753°W. The nearly isothermal sound-speed profile measured by a conductivity, temperature, and density (CTD) cast during the experiment is shown in Fig. 2.2.

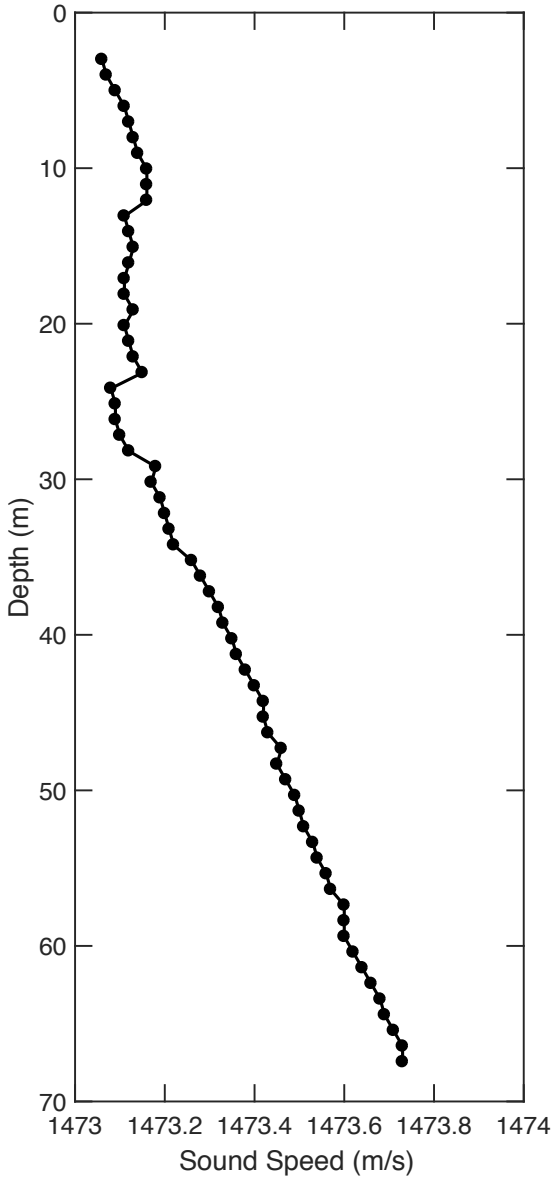

Figure 2.2: Sound-speed profile measured by CTD cast at the experiment site.

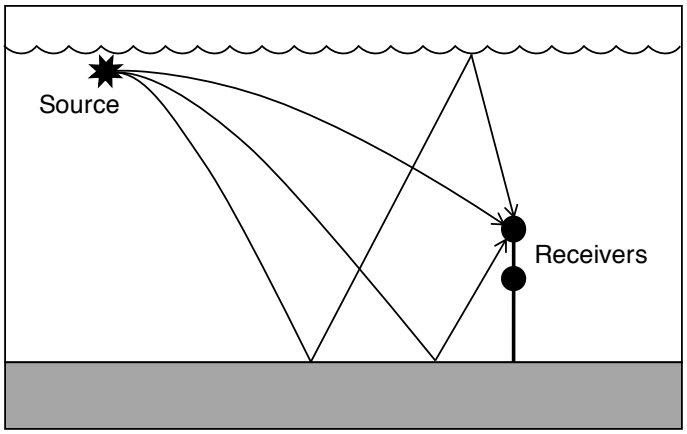

Figure 2.3: Experiment geometry showing the direct, bottom-reflected, and bottom-surface-reflected paths. The data considered are for a tow that passed nearly overtop of the receivers, starting at an approximate range of 1000 m, ending at a range of ∼600 m.

The survey geometry, illustrated in Fig. 2.3, was designed to implement the reflection-coefficient measurement technique developed by Holland and Osler [21]. The survey involved two bottom-moored omni-directional receivers and a broadband Uniboom source towed behind a ship along a ∼1.6-km radial track in approximately 76 m of water. The receivers were positioned at nominal depths of 61 and 65 m, far enough above the seabed to prevent interference between the direct and bottom-reflected acoustic arrivals. The source was mounted to a catamaran equipped with GPS and towed at a depth of ∼0.4 m, thus allowing the direct and sea-surface-reflected acoustic arrivals to be considered as one waveform. The source emitted a short pulse (<1 ms) with a broad bandwidth (0.1–10 kHz) every second. The ship speed was approximately 3 knots (1.5 m/s). An initial estimate of the deployment location of the receivers was estimated by using an Ultra Short Baseline system where one transponder was near the base of the mooring and the other transponder was on a pole deployed beneath the ship. Each receiver had its own clock which was synchronized with GPS on-board ship; however, the clocks drifted at different and unknown rates following deployment. Hence, absolute travel time between the source transmission and signal arrival at the receiver could not be directly measured. Accordingly, synchronization corrections were included as unknown parameters in the inversion.

The data used for the high-precision geometry inversion include the acoustic arrival times for the direct, bottom-reflected, and surface-bottom-reflected paths at the receivers picked from the recorded time series. The acoustic data are treated as absolute arrival times along direct and reflected paths relative to the (unknown) source

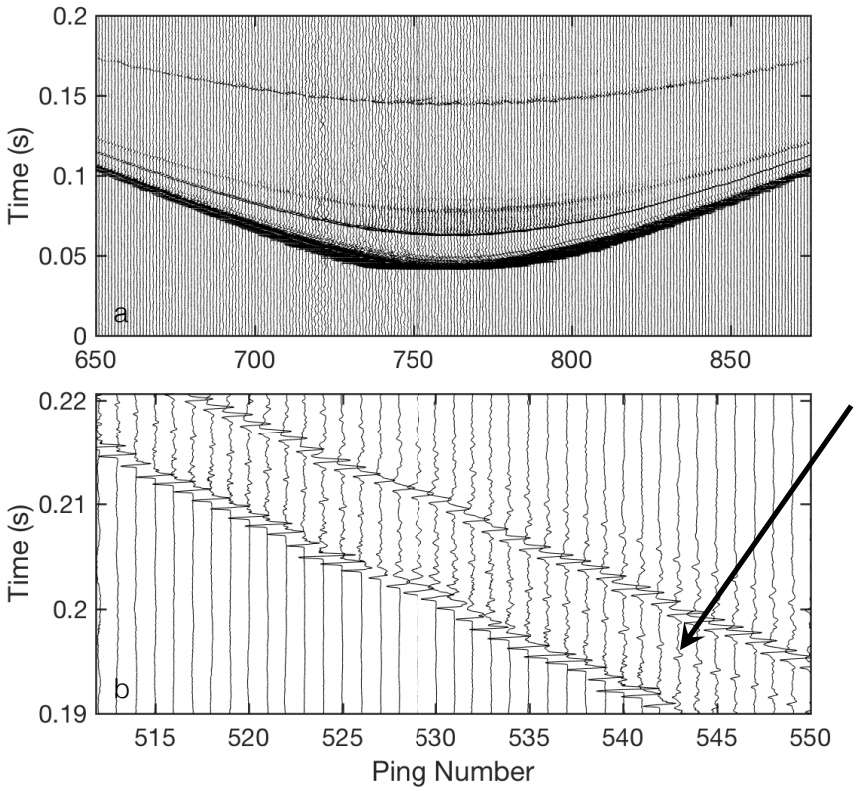

Figure 2.4: Acoustic time series for the shallow receiver. (a) shows a section of data near CPA. The four distinct arrivals (from earliest to latest) are the direct path, bottom-reflected path, sub-bottom-reflected path, and bottom-surface-reflected path arrivals. (b) shows the first three arrivals at longer ranges, with the arrow indicating the bottom-reflected arrival.

transmission instants. With knowledge that successive source transmissions were separated by precisely 1 s (pulse repetition rate), only the initial source transmission instant is included as an unknown parameter in the inversion. This allows direct-path arrival times to provide useful data even at longer ranges where reflected arrivals were difficult to distinguish and only direct arrivals could be picked. Fig. 2.4(a) shows time series recorded near CPA which include four distinct arrivals that are, from earliest to latest: the direct, bottom-reflected, sub-bottom-reflected, and bottom-surface-reflected paths. Fig. 2.4(b) shows a close up of the first three arrivals at longer ranges (prior to CPA). Here, the bottom-reflected arrivals (indicated with the arrow) are much weaker than the sub-bottom arrivals which follow. At even longer ranges, the bottom-reflected arrivals become difficult to identify and pick. A total of 1197 source transmissions (i.e., pings) were recorded over a 20-minute period. The direct arrivals were picked by searching for the largest peak along the time series. The reflected-path

Table 2.1
Summary of data and prior uncertainty estimates for linearized Bayesian inversion.

Data/Parameter (Units)	Standard deviation
Direct arrival (s)	0.0002
Bottom-reflected arrival (s)	0.0003
Bottom-surface-reflected arrival (s)	0.001
Range, r (m)	100
Source depth, z_i (m)	0.5
Water depth, W (m)	0.5
Receiver depth, z_j (m)	1.0
Synchronization correction, τ_j (s)	0.001

arrivals were picked by windowing the direct arrival waveform and cross-correlating the windowed signal along the time series. The bottom-reflected and bottom-surface-reflected arrivals become increasingly indistinct at long ranges, as illustrated for the bottom-reflected arrival in Fig. 2.4(b). Therefore, the reflected arrivals were confidently picked between pings 550 and 949 (or about 265 and 230 m) while the direct arrivals were picked for all 1197 pings. In total, including both receivers, 2394 direct, 800 bottom-reflected, and 800 bottom-surface-reflected arrivals were picked for a total of $N = 3994$ acoustic arrival-time data for the inversion.

Using this data set, the inversion seeks to estimate 1197 source-receiver ranges, 1197 source depths, 400 water depths for the bottom-reflected paths, 400 water depths for the bottom-surface-reflected paths, 2 receiver depths, and 2 receiver synchronization corrections for a total of $M = 3198$ model parameters. Water depths can only be estimated for the centre 400 pings given that the arrivals that interact with the seafloor were only picked for this region.

The prior information applied in the Bayesian inversion consists of Gaussian prior densities for each parameter based on a prior estimate and uncertainty (standard deviation). The prior model estimates are taken from GPS, bathymetry, and available knowledge of the experiment geometry setup. The uncertainties assigned to these prior estimates and to the data are given in Table 2.1. The range uncertainties are intentionally over-estimated for two reasons. First, the uncertain location of the receivers on the seabed represents a bias in the prior information for range, i.e., all prior range estimates along the track are affected by this error in the same way; one way to accommodate this bias is to increase uncertainties. Second, ranges (and grazing angles) are the most important parameters required for reflection-coefficient estimation, and we prefer to have the data, rather than the prior, primarily constrain

these. Note that the acoustic data may not have sufficient information to estimate all parameters (e.g., source depths and water depths) beyond their prior, but including these parameters in the inversion includes the effect of their uncertainties in the uncertainty estimates for the ranges (and grazing angles).

2.3 Theory and Algorithms

2.3.1 Forward Problem: Ray tracing

This section summarizes the ray-tracing forward model and ray derivatives used in the inversion algorithm [41–43]. The range r and arrival time t between source i and receiver j along a non-turning direct ray (i.e., a ray that does not change vertical direction as the result of reflection or refraction) is given by

$$r = \int_{z_i}^{z_j} \frac{pc(z)\,\mathrm{d}z}{[1 - p^2c^2(z)]^{1/2}}, \tag{2.1}$$

$$t = \tau_j + \int_{z_i}^{z_j} \frac{\mathrm{d}z}{c(z)[1 - p^2c^2(z)]^{1/2}}, \tag{2.2}$$

where τ_j represents the time correction to synchronize receiver and source, $c(z)$ is the water sound speed as a function of depth z, and p is the ray parameter (constant along a ray path) given by

$$p = \frac{\cos\theta(z)}{c(z)}, \tag{2.3}$$

where $\theta(z)$ is the ray grazing angle at depth z. The ray parameter for an eigenray connecting source and receiver is determined by searching for the value of p which produces the correct range (to a specific tolerance) according to (2.1).

Dosso and Ebbeson [42] developed an efficient procedure to determine p applying Newton's method. An initial estimate p_0, calculated for straight-line propagation with constant sound speed, is given by

$$p_0 = \frac{r}{c_H[r^2 + (z_j - z_i)^2]^{1/2}}, \tag{2.4}$$

where c_H is the harmonic mean sound speed over the propagation path given by

$$c_H = (z_j - z_i) \Big/ \int_{z_i}^{z_j} \frac{\mathrm{d}z}{c(z)}. \tag{2.5}$$

An improved estimate p_1 is obtained by expanding $r(p)$ in a Taylor series about p_0 neglecting second-order terms leading to

$$p_1 = p_0 + \left[\frac{\partial r(p_0)}{\partial p}\right]^{-1} (r(p) - r(p_0)). \tag{2.6}$$

In (2.6), $\partial r/\partial p$ is determined by differentiating (2.1) according to Leibnitz's rule to yield [42]

$$\frac{\partial r}{\partial p} = \int_{z_i}^{z_j} \frac{c(z)\,\mathrm{d}z}{[1 - p^2 c^2(z)]^{3/2}}. \tag{2.7}$$

If $r(p_1)$ calculated from (2.1) is within the desired range tolerance (10^{-5} m was used here), the procedure is considered complete. If not, the starting value is updated $p_0 \leftarrow p_1$ and the procedure is repeated iteratively until a satisfactory value is obtained. For reflected paths, this formulation can be applied by treating sea-surface and bottom reflections as direct rays using the method of images (i.e., by representing the reflected ray path by a direct path from an image source located above the surface or below the bottom).

The linearized inversion in Section 2.3.2 requires the computation of partial derivatives of acoustic arrival-times t with respect to the unknown model parameters. These partial derivatives can be derived analytically and are given by [41, 42, 45]

$$\frac{\partial t}{\partial r} = p_1, \tag{2.8}$$

$$\frac{\partial t}{\partial z_i} = -\frac{1}{c(z_i)}[1 - p^2 c^2(z_i)]^{1/2}, \tag{2.9}$$

$$\frac{\partial t}{\partial z_j} = \frac{1}{c(z_j)}[1 - p^2 c^2(z_j)]^{1/2}, \tag{2.10}$$

for the direct and bottom-surface-reflected arrivals, and

$$\frac{\partial t}{\partial z_j} = -\frac{1}{c(z_j)}[1 - p^2 c^2(z_j)]^{1/2}, \tag{2.11}$$

for the bottom-reflected arrival. For water depth W

$$\frac{\partial t}{\partial W} = \frac{2}{c(W)}[1 - p^2 c^2(W)]^{1/2}, \tag{2.12}$$

for the reflected arrivals and zero for the direct arrival. Lastly, for all paths

$$\frac{\partial t}{\partial \tau_j} = 1. \tag{2.13}$$

However, in this work, τ_j in (2.2) is replaced by $(\bar{c}\tau_j)/\bar{c}$ such that $\bar{c}\tau_j$ is considered the unknown parameter, where $\bar{c}$ represents a representative sound speed (1500 m/s here). This scales the unknown synchronization time correction to the same physical units (distance) and similar uncertainty as the other model parameters, thereby improving the numerical stability of the inversion algorithm [42]. In this case, the partial derivative becomes

$$\frac{\partial t}{\partial (\bar{c}\tau_j)} = \frac{1}{\bar{c}}. \tag{2.14}$$

The integrals in (2.1), (2.2), (2.5), and (2.7) are evaluated analytically by assuming that a discrete sound-speed profile can be represented by a series of layers with a (non-zero) linear gradient in each layer. Let $\left\{(z_k, c_k), k = 1, N_z\right\}$ represent the piece-wise linear sound-speed profile and $\{g_k\}$ the corresponding layer sound-speed gradient, then,

$$r = \sum_{k=i}^{j-1} \frac{w_k - w_{k+1}}{p\, g_k}, \tag{2.15}$$

$$t = \tau_j + \sum_{k=i}^{j-1} \frac{1}{g_k} \left[\log_{\mathrm{e}} \frac{c_{k+1}\,(1 + w_k)}{c_k\,(1 + w_{k+1})} \right], \tag{2.16}$$

$$c_H = (z_j - z_i) \Bigg/ \sum_{k=i}^{j-1} \frac{1}{g_k} \left[\log_{\mathrm{e}} \frac{g_k\,(z_{k_1} - z_k) + c_k}{c_k} \right], \tag{2.17}$$

$$\frac{\partial r}{\partial p} = \sum_{k=i}^{j-1} \frac{w_k - w_{k+1}}{p^2\, g_k\, w_k\, w_{k+1}}, \tag{2.18}$$

where $w_k \equiv (1 - p^2 c_k^2)^{1/2}$.

2.3.2 Linearized Bayesian Formulation

Although fully-nonlinear methods are often applied to solve Bayesian inverse problems, linearization can be applied to weakly nonlinear problems and can provide much more efficient approximate solutions [42, 46–48]. To present this approach, consider first the linear inverse problem

$$\mathbf{d} = \mathbf{A}\mathbf{m}, \tag{2.19}$$

where $\mathbf{d}$ and $\mathbf{m}$ are vectors of data and model parameters, respectively, and $\mathbf{A}$ is the Jacobian (or sensitivity) matrix containing the physics of the forward problem given by

$$A_{ij} = \frac{\partial d_i}{\partial m_j}, \tag{2.20}$$

for $i = 1, \ldots, N$ data and $j = 1, \ldots, M$ model parameters. Assuming $\mathbf{m}$ and $\mathbf{d}$ to be random variables, they are related through Bayes' rule [23]

$$P(\mathbf{m}|\mathbf{d}) \propto P(\mathbf{d}|\mathbf{m})P(\mathbf{m}). \tag{2.21}$$

In (2.21), $P(\mathbf{m})$ is the prior density representing knowledge about $\mathbf{m}$ independent of $\mathbf{d}$. $P(\mathbf{d}|\mathbf{m})$, when interpreted as a function of $\mathbf{d}$, represents the data uncertainty distribution. However, for the observed (fixed) data, $P(\mathbf{d}|\mathbf{m})$ can be interpreted as a function of $\mathbf{m}$, which defines the likelihood function. Finally, $P(\mathbf{m}|\mathbf{d})$ is the posterior probability density (PPD), representing the total information about the model including both data and prior information. Assuming the data errors are zero-mean, Gaussian-distributed random variables with data covariance matrix $\mathbf{C}_d$ and a Gaussian prior density about a prior model estimate $\mathbf{m}_p$ with prior model covariance matrix $\mathbf{C}_p$, the PPD can be expressed as

$$\begin{aligned} P(\mathbf{m}|\mathbf{d}) \propto \exp\Bigg[-\frac{1}{2}\Big\{ &(\mathbf{d} - \mathbf{A}\mathbf{m})^T \mathbf{C}_d^{-1} (\mathbf{d} - \mathbf{A}\mathbf{m}) \\ &+ (\mathbf{m} - \mathbf{m}_p)^T \mathbf{C}_p^{-1} (\mathbf{m} - \mathbf{m}_p) \Big\} \Bigg], \end{aligned} \tag{2.22}$$

where $(\cdot)^T$ represents transpose. The most probable or maximum *a posteriori* (MAP) model $\hat{\mathbf{m}}$ is obtained by setting $\partial P(\mathbf{m}|\mathbf{d})/\partial \mathbf{m} = 0$ leading to

$$\hat{\mathbf{m}} = \mathbf{m}_p + [\mathbf{A}^T \mathbf{C}_d^{-1} \mathbf{A} + \mathbf{C}_p^{-1}]^{-1} \mathbf{A}^T \mathbf{C}_d^{-1} [\mathbf{d} - \mathbf{A}\mathbf{m}_p]. \tag{2.23}$$

The PPD is represented by an M-dimensional Gaussian probability density centered at $\hat{\mathbf{m}}$ with posterior model covariance matrix [23]

$$\hat{\mathbf{C}}_m = [\mathbf{A}^T \mathbf{C}_d^{-1} \mathbf{A} + \mathbf{C}_p^{-1}]^{-1}. \tag{2.24}$$

The inverse problem of estimating experiment geometry from acoustic arrival-times is nonlinear. However, a local linearization is achieved by expanding $\mathbf{d} = \mathbf{d}(\mathbf{m})$ in a generalized Taylor series about an arbitrary starting model $\mathbf{m}_0$ and neglecting

second-order terms leading to

$$\mathbf{d} = \mathbf{d}(\mathbf{m}_0) + \mathbf{A}(\mathbf{m} - \mathbf{m}_0), \tag{2.25}$$

with the Jacobian derivatives estimated at the starting model

$$A_{ij} = \frac{\partial d_i(\mathbf{m}_0)}{\partial m_j}. \tag{2.26}$$

The MAP solution to the linearized inverse problem in (2.25) is then given by

$$\hat{\mathbf{m}} = \mathbf{m}_p + [\mathbf{A}^T\mathbf{C}_d^{-1}\mathbf{A} + \mathbf{C}_p^{-1}]^{-1}\mathbf{A}^T\mathbf{C}_d^{-1}[\mathbf{d} - \mathbf{d}(\mathbf{m}_0) + \mathbf{A}(\mathbf{m}_0 - \mathbf{m}_p)]. \tag{2.27}$$

Since nonlinear terms are neglected, the linearized inversion is repeated iteratively until convergence. To stabilize the linearized iterations by keeping steps small and controlled, a trade-off parameter μ is incorporated such that the MAP model is obtained by iterating

$$\hat{\mathbf{m}} = \mathbf{m}_p + [\mathbf{A}^T\mathbf{C}_d^{-1}\mathbf{A} + \mu\,\mathbf{C}_p^{-1}]^{-1}\mathbf{A}^T\mathbf{C}_d^{-1}[\mathbf{d} - \mathbf{d}(\mathbf{m}_0) + \mathbf{A}(\mathbf{m}_0 - \mathbf{m}_p)], \tag{2.28}$$

where μ starts at a high value (e.g., 1000 here) and is decreased to unity over the set of iterations leading to the MAP solution (2.27) (typically, 10 iterations provided good convergence for the cases considered here).

The linearized approximation to the PPD is a Gaussian distribution about $\hat{\mathbf{m}}$ with posterior model covariance matrix [23]

$$\hat{\mathbf{C}}_m = [\mathbf{A}^T\mathbf{C}_d^{-1}\mathbf{A} + \mathbf{C}_p^{-1}]^{-1}, \tag{2.29}$$

where $\mathbf{A}$ is evaluated at the final model estimate $\hat{\mathbf{m}}$. The square root of the diagonal elements of $\hat{\mathbf{C}}_m$ provide standard deviation (uncertainty) estimates for the model parameters.

2.3.3 Track Prediction Prior

It was found that the linearized algorithm described in the previous section provided poor results (large uncertainties) for source-receiver range estimates near CPA, indicating the data have little information to constrain ranges here. The low data information is due to near-zero $\partial t/\partial r$ sensitivities for near-vertical ray paths which occur near CPA. To address this problem, more-accurate estimates for ranges near

CPA are determined using a track prediction algorithm [44] to augment the prior where data information is low.

The track-prediction approach makes use of a set of ranges estimated by the linearized inversion for source locations along the track where the data information content is high (farther from CPA) to predict ranges where the information is low (near CPA). The model for predicting ranges $R(t)$ near CPA is given by

$$R(t) = \Big[(x_0 - vt)^2 + R_{\rm CPA}^2\Big]^{1/2}, \tag{2.30}$$

where x_0 represents the distance along the track from CPA to the point where the track model is initiated, with time t set to zero at this point. The parameter v is the ship speed (assumed constant over the track segment considered), and $R_{\rm CPA}$ is the range at CPA.

The track prediction algorithm used 30 estimated range points at $>$ 25 m on each side of CPA (obtained from the previous linearized inversion step) as data $\mathbf{d}$ to estimate the track model $\mathbf{m} = [x_0, v, R_{\rm CPA}]^T$. Subsequently, these model parameters were used to predict 40 range points for the region between $\sim$25 m before to 25 m past CPA. The range-prediction approach is illustrated in Fig. 2.5. In this figure, the inaccurate range estimates near CPA are represented by crosses, the ranges used as data in estimating the track model are represented by filled circles and the predicted range points are represented by open circles. An iterative linearized approach is used to compute the track model parameters $\hat{\mathbf{m}}$ similar to (2.27) but without the use of prior information since the problem is strongly overdetermined, i.e.,

$$\hat{\mathbf{m}} = [\mathbf{A}^T\mathbf{C}_d^{-1}\mathbf{A}]^{-1}\mathbf{A}^T\mathbf{C}_d^{-1}[\mathbf{d} - \mathbf{d}(\mathbf{m}_0) + \mathbf{A}\mathbf{m}_0], \tag{2.31}$$

where the columns of the $N \times 3$ Jacobian matrix $\mathbf{A}$ in (2.31) are given by

$$\mathbf{A}_{i1} = \frac{\partial R_i}{\partial x_0} = (x_0 - v\,t_i)\Big[(x_0 - v\,t_i)^2 + R_{\rm CPA}^2\Big]^{-1/2}, \tag{2.32}$$

$$\mathbf{A}_{i2} = \frac{\partial R_i}{\partial v} = t_i\,(v\,t_i - x_0)\Big[(x_0 - v\,t_i)^2 + R_{\rm CPA}^2\Big]^{-1/2}, \tag{2.33}$$

$$\mathbf{A}_{i3} = \frac{\partial R_i}{\partial R_{\rm CPA}} = R_{\rm CPA}\Big[(x_0 - v\,t_i)^2 + R_{\rm CPA}^2\Big]^{-1/2}, \tag{2.34}$$

where N represents the 60 range values used to define the track model parameters, and $\mathbf{C}_d$ is a diagonal matrix with variances on the main diagonal corresponding to standard deviations of 0.5 m (roughly the range uncertainties from the arrival-

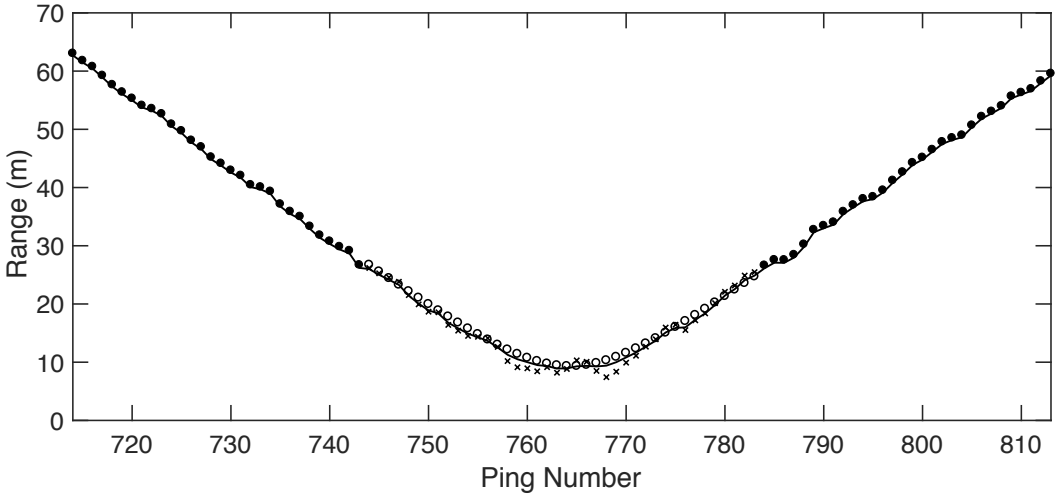

Figure 2.5: Procedure for augmenting the range prior through CPA based on track predictions. The inaccurate initial range estimates through CPA from arrival-time inversion are shown by crosses. The more-stable initial range estimates further from CPA from the same inversion, shown by filled circles, are used to determine the track-prediction model parameters. The augmented prior estimates near CPA determined via track prediction are shown by open circles. The final estimates for all ranges computed by incorporating the augmented prior in the linearized inversion are shown by the solid line.

time inversion). The resulting MAP parameters for the track-prediction model were subsequently used to estimate source-receiver ranges $R(t)$ along the track segment through CPA according to (2.30). The range prior was then updated with the 40 predicted range points near CPA and the prior model uncertainties for these ranges were reduced to 2 m. Finally, with the updated prior, the linearized Bayesian inversion of acoustic arrival-time data was re-run. The final inversion results obtained with the augmented prior near CPA is represented by the line in Fig. 2.5. As shown in this figure, the final inversion results do not include the unphysical fluctuations in range that were present in the initial arrival-time inversion (crosses).

2.3.4 Grazing Angles and Uncertainties

The calculation of reflection coefficients requires seabed reflection (grazing) angles as well as ranges. The grazing angles along the track are computed using ray tracing and the estimated experiment geometry according to (2.3) evaluated at $z = W$, where W is the water depth at the reflection point. The estimated water depths for the centre 400 pings are used to calculate the centre 400 grazing angles while

an average water depth is used for all other grazing angle calculations. The grazing angle uncertainties, based on experiment geometry uncertainties, are computed using a Monte Carlo approach. This nonlinear procedure involves drawing a large number of random samples (1000 was used here) from the experiment-geometry PPD, calculating grazing angles for each random model, and computing the standard deviations for the ensemble of grazing angles.

2.4 Results

This section presents the results of the linearized Bayesian inversion of acoustic arrival-time data for high-precision estimation of experiment geometry and grazing angles. Fig. 2.6 illustrates the fit to the data for the direct, bottom-reflected, and bottom-surface-reflected arrivals for the shallow receiver. The figure shows excellent agreement between observed and predicted arrival times, with small residuals (differences between observed and predicted data) in all cases. The apparent discretization in the residuals is due to the finite precision of the measured data (0.01 ms).

Fig. 2.7 shows the results in terms of estimated ranges and grazing angles and their uncertainties. At the start of the survey, the source-receiver range is found to be 977 $\pm$ 0.23 m and the calculated grazing angle for the bottom-reflected path is 5.2 $\pm$ 0.03°. At CPA, the source-receiver range is 9 $\pm$ 1.8 m and the grazing angle is 84 $\pm$ 1°. The final source-receiver range is 570 $\pm$ 0.23 m with a grazing angle of 9 $\pm$ 0.05°. The small jumps in range and grazing angle uncertainties at ping number 744 and 784 are due to the augmented prior used through this portion of the track. The small jumps in range and grazing angle uncertainties at ping number 550 and 949 are due to the fact that water depths were only estimated for the centre 400 source transmissions.

The remainder of the inversion results are summarized as follows. The average source depth along the track determined by inversion is 0.39 m with an uncertainty of 0.49 m (computed as the root mean square (RMS) of the source-depth standard deviations along the track). These results are almost identical to the prior information, indicating that the data had little ability to resolve source depths beyond the prior in this problem. Nonetheless, incorporating source depths as unknown parameters in the inversion accounts for source-depth uncertainties in the range and grazing angle uncertainty estimates. The average water depth for the bottom-reflected paths determined by inversion is 76.1 m with an RMS uncertainty of 0.28 m. No significant variation of water depth along the track was detected. The mean water depth value agrees

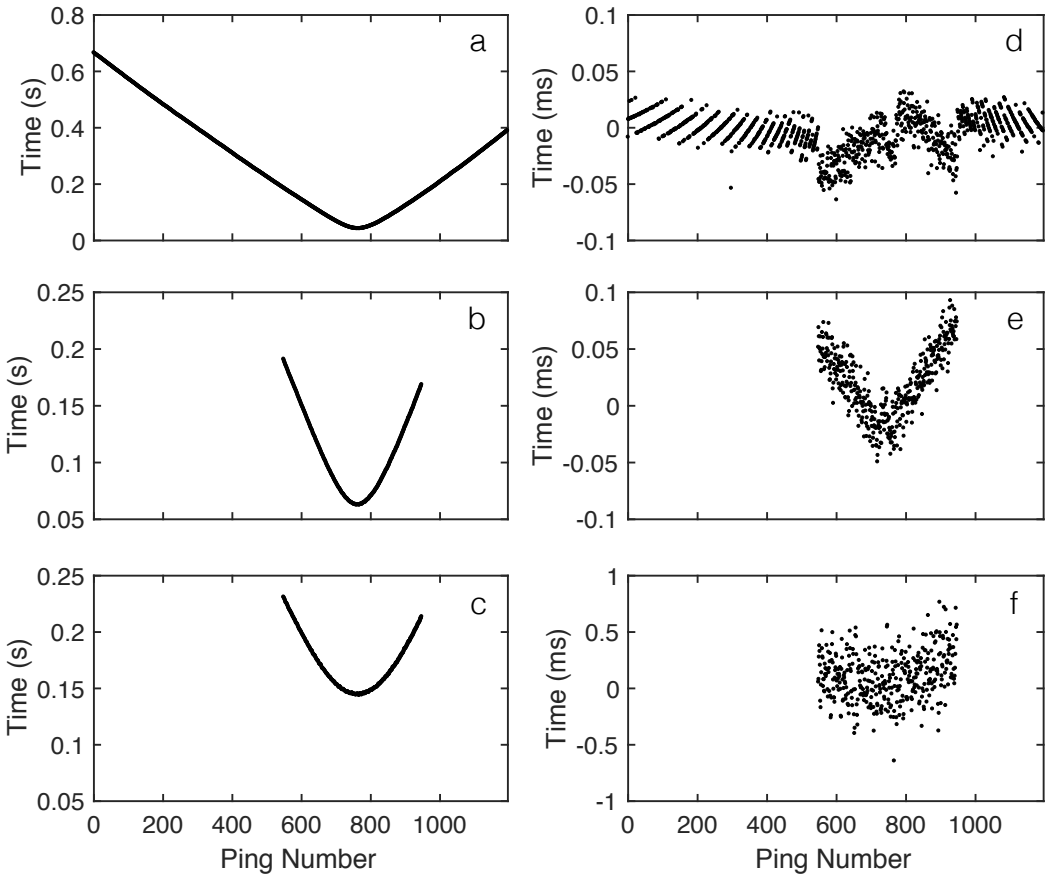

Figure 2.6: Fit to the data for the direct, bottom-reflected, and bottom-surface-reflected paths for the shallow receiver are shown in (a), (b), and (c), respectively. In these panels, filled circles represent observed data and the line is the predicted data (indistinguishable). (d), (e), and (f) present the corresponding residuals (differences between observed and predicted data).

with the expected value based on bathymetry measurements taken at the survey site. The uncertainties are slightly smaller than the prior uncertainties. The depths and uncertainties for the shallow and deep receivers, determined by inversion, are 60.2 $\pm$ 0.05 m and 64.5 $\pm$ 0.05 m, respectively. Finally, the synchronization corrections for the shallow and deep receivers, determined by inversion, are 0.48 $\pm$ 6×10^{-5} s and 0.69 $\pm$ 6×10^{-5} s, respectively.

2.5 Monte Carlo Uncertainty Analysis

The previous section described linearized uncertainty estimates which can be evaluated efficiently from the linearized solution. Monte Carlo [23] appraisal provides an

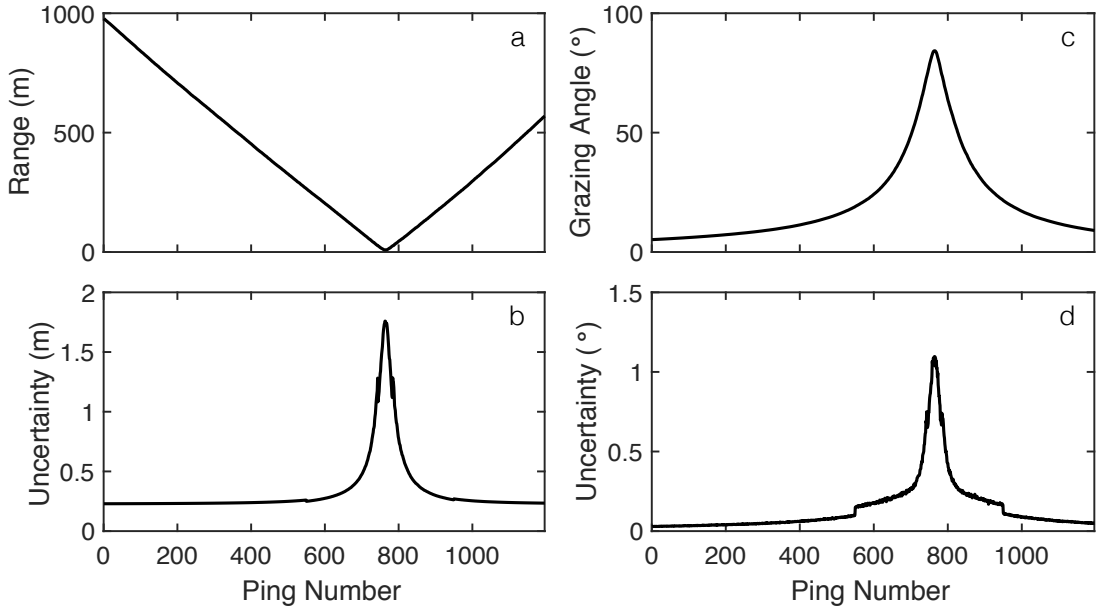

Figure 2.7: Results and uncertainties for ranges and grazing angles. (a) and (c) show the results for ranges and grazing angles, respectively. (b) shows the linearized uncertainties for range and (d) shows the uncertainties obtained via nonlinear Monte Carlo approach for grazing angles.

alternate approach which provides fully nonlinear uncertainty estimates, but is much more computationally intensive. The Monte Carlo approach is applied here to verify that linearization errors are small in the acoustic inversion results. In the Monte Carlo approach, the experiment geometry determined by inversion of the measured data is assumed to define the true model for a synthetic inverse problem, and acoustic arrival-time data are computed for this synthetic model using ray theory. A series of independent inversions are then carried out, each with different random errors applied to the computed data, the prior estimates, and the starting model (these errors are drawn from Gaussian distributions with standard deviations equivalent to the corresponding estimated uncertainties of the data and priors from Table 2.1). Error distributions and standard deviations can then be computed from the ensemble of inversion results providing fully nonlinear uncertainty estimates.

Fig. 2.8 shows reasonably close agreement between Monte Carlo uncertainty analysis (Fig. 2.8(a) and 2.8(c)) and inversion results (Fig. 2.8(b) and 2.8(d)) for grazing angles and ranges with estimated one standard-deviation uncertainties on both quantities indicated by error bars. The RMS error between mean Monte Carlo and inversion results for range is 0.08 m and for grazing angles is 0.07°. The RMS standard deviation for range determined by Monte Carlo is 0.4 m and by inversion 0.4 m.

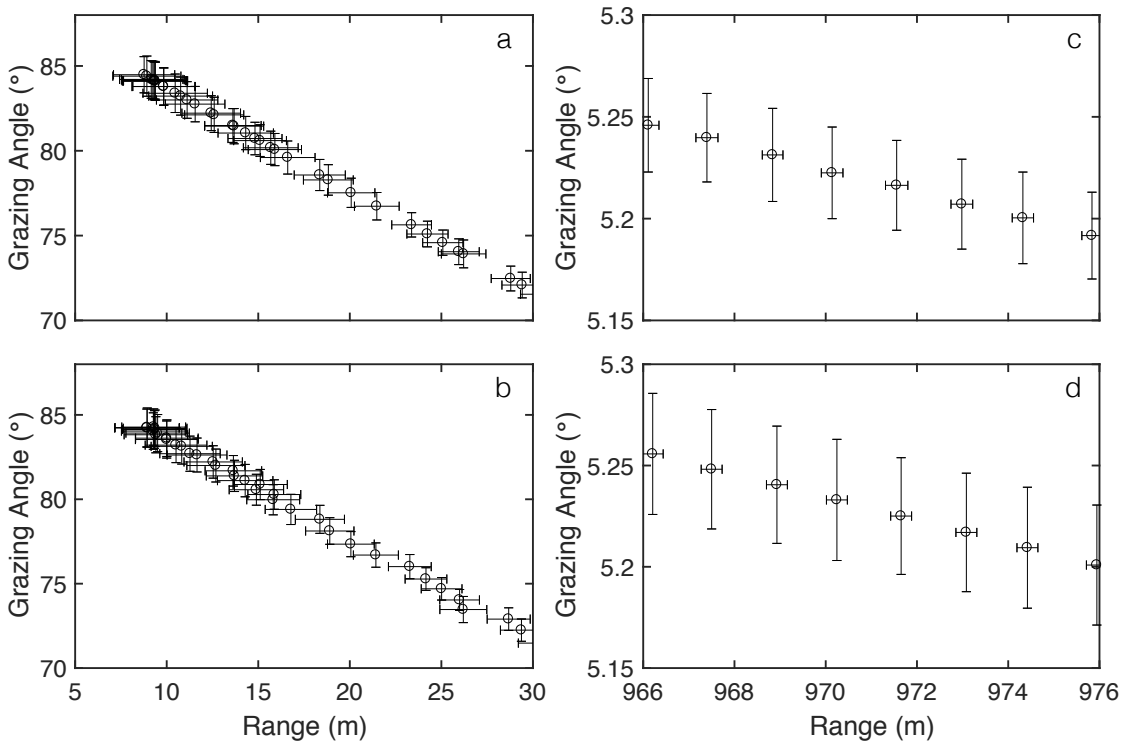

Figure 2.8: Monte Carlo uncertainty analysis and inversion results. A comparison of grazing angle versus range with uncertainties (one-standard deviation error bars) for the shallow receiver between Monte Carlo uncertainty analysis in (a) and (c) and inversion results in (b) and (d), for short-range and long-range track segments.

For grazing angles, the Monte Carlo analyses produced close RMS standard deviations of 0.23° (computed for linearized inversion) and 0.28° (Monte Carlo estimate). This close agreement indicates that the linearization errors are small and that linearization provides a useful and efficient method for estimating experiment geometry uncertainties.

Fig. 2.9 compares Monte Carlo uncertainty normalized distributions (computed from the ensemble of solutions) to the analytic marginal PPDs from the linearized inversion of the measured data for six selected ranges along the track. The generally good agreement between nonlinear and linearized analysis indicates that the linearized Bayesian approach is well justified. Finally, it is worth noting that the Monte Carlo approach based on 1000 iterations took roughly 1000 times longer than the linearized inversion in computing uncertainty estimates.

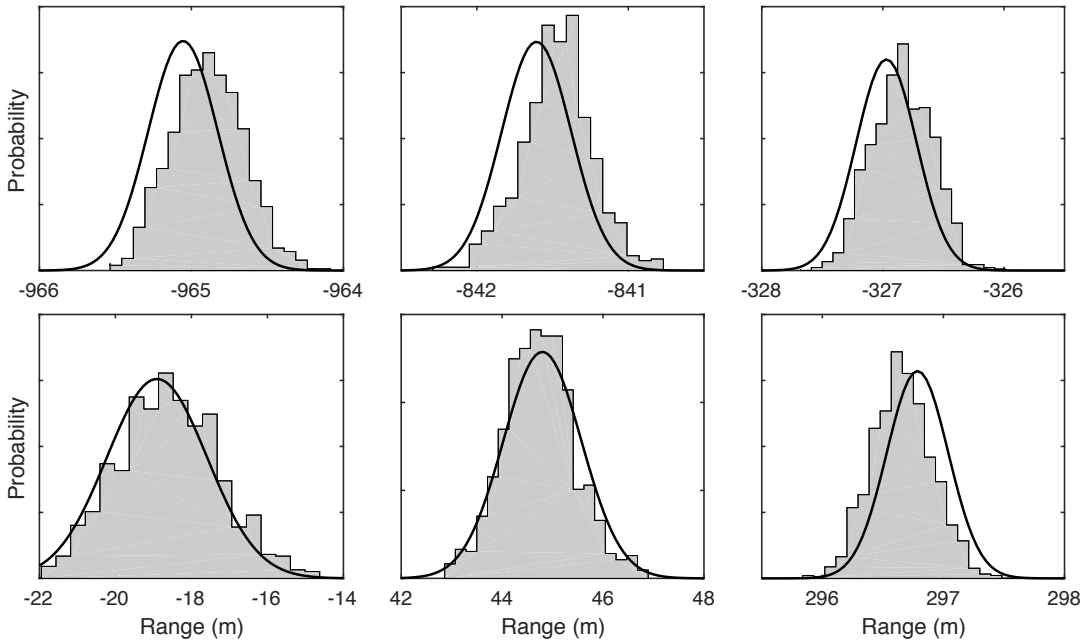

Figure 2.9: Comparison of Monte Carlo uncertainty distributions to analytic marginal probability densities from the linearized inversion of measured data (smooth curves) for six selected ranges. The negative ranges represent source-receiver ranges before CPA (i.e., inbound leg).

2.6 Summary and Discussion

This chapter presented linearized Bayesian inversion of acoustic arrival-time data for high-precision estimation of experiment geometry and grazing angles and uncertainties at the SWAMI site. The approach is based on inversion of the acoustic ray-tracing equations accounting for uncertainties in the data and prior estimates for source-receiver ranges, source depths, receiver depths, water depths for bottom-reflected paths, and receiver synchronization corrections. The Bayesian formulation incorporates prior estimates from GPS and bathymetry measurements. Track predictions are used to provide improved range priors near CPA where the data information is low. Posterior uncertainties are estimated efficiently from the linearized model covariance matrix. The model parameters are used to calculate grazing angles along the track with angle uncertainties determined by Monte Carlo methods. The uncertainties obtained using analytic linearized estimates for the model parameters are verified with a fully nonlinear Monte Carlo appraisal procedure.

The high-precision estimation of experiment geometry and uncertainties are required for reflection-coefficient measurements and Bayesian geoacoustic inversion of

reflection-coefficient data at the New England Mud Patch. However, the methods presented here are general and can be used in other applications where accurate source and receiver locations and/or experiment geometry are required.

Chapter 3

Trans-dimensional Bayesian Geoacoustic Inversion of Reflection Coefficients at the New England Mud Patch

This chapter presents nonlinear Bayesian geoacoustic inversion for fine-grained/cohesive sediments recorded in the U.S. Office of Naval Research (ONR) Seabed Characterization Experiment 2017 (SCBEX) at the New England Mud Patch. In particular, the inversion is applied to high-resolution broadband reflection-coefficient data from two sites of contrasting mud-layer thicknesses. Trans-dimensional (trans-D) inversion, sampling over an unknown number of seabed interfaces and parameters of a zeroth- or first-order autoregressive error model, is employed with forward modelling based on spherical-wave (full-wave) reflection coefficients. The inversion provides marginal posterior probability profiles for Buckingham's viscous grain-shearing (VGS) parameters: porosity, grain-to-grain compressional modulus, material exponent, and compressional viscoelastic time constant as a function of depth in the sediment. The VGS parameters are used to compute dispersion relationships for each layer in the model to yield compressional-wave velocity and attenuation as functions of frequency, as well as marginal posterior probability profiles for compressional-wave velocity and attenuation at different frequencies, and density. Results of the geoacoustic inversion are compared to independent measurements of sediment properties collected at the experiment sites.

The data presented here were collected at sea by Charles W. Holland, who also computed the reflection coefficients using previously-developed methods [21]. Jan

Dettmer provided the computer algorithms used in carrying out the trans-D inversion. The author of this thesis further processed the frequency-averaged data, carried out the inversions to produce the results presented here, and wrote the paper on which this chapter is based.

3.1 Introduction

Inferring seabed geoacoustic model parameters from ocean acoustic measurements has received considerable attention over the years, e.g., [49–53]. This approach represents an economical alternative to direct measurements (e.g., coring) with many geotechnical, geologic, and sonar applications. However, geoacoustic inversion requires solving an inherently nonunique, nonlinear inverse problem, and necessitates rigorous estimations of data and model uncertainties, e.g., [10, 11, 32, 37]. As such, two of the main objectives of SBCEX at the New England Mud Patch, a major collaborative study funded by ONR, are to quantify uncertainties in seabed parameters estimated by geoacoustic inversion and assess the resulting geoacoustic models and inversion methods [17]. This chapter applies a trans-D Bayesian geoacoustic inversion of seabed reflection-coefficient data for fine-grained/cohesive (muddy) sediments for two locations at the New England Mud Patch.

Reflection coefficients represent the ratio of the amplitudes of a reflected wave to a wave incident on an interface separating two media of different physical properties [2], and are a highly informative measure of the effect of the bottom on sound propagation. The measurement geometry for the data considered here involved an impulsive broadband acoustic source towed near the surface of the water, and two omni-directional receivers moored far enough above the seabed to prevent interference from direct- and bottom-reflected acoustic paths. The reflection coefficients are computed from time-windowed acoustic arrivals and corrected for various experimental effects (e.g., source directivity, geometric spreading, and absorption) [21, 22].

In a Bayesian inversion formulation, the statistical distribution of the data errors, including both measurement and theory errors, must be specified, but is often not a well known *a priori*. Moreover, the theory errors (e.g., due to model parameterization and approximations of the forward problem) are generally difficult to estimate independently and can strongly influence model uncertainty estimates. For example, the model parameterization (e.g., number of seabed interfaces), if under-parametrized, can lead to under-estimating uncertainties [14]. Conversely, if the model parameterization is over-parameterized, the model can over-fit the data and over-estimate

uncertainties. In many cases, lack of knowledge suggests that a simple error distribution (e.g., Gaussian) be assumed, with statistical parameters estimated from the data. This chapter applies a trans-D Bayesian formulation of the inverse problem to sample the posterior probability density (PPD) of geoacoustic parameters for an unknown number of seabed interfaces and parameters of a zeroth- or first-order autoregressive error model [10, 11, 32, 37]. The unknown standard deviations of the assumed Gaussian distributed errors plus coefficients of the autoregressive model of error correlations are sampled explicitly as additional (nuisance) parameters in the inversion. This approach provides marginal posterior probability profiles for geoacoustic parameters with uncertainties that include the model parametrization, and accounts for error covariance, avoiding over- or under-parameterizing the error model.

The trans-D PPD is sampled numerically using reversible-jump Markov-chain Monte Carlo (rjMCMC) methods [33, 34] that jump between subspaces of different dimensions (number of parameters) using a birth-death scheme to add/remove interfaces [35]. Fixed-dimensional perturbation steps are proposed in a principal-component (PC) parameter space providing both directions and length scales for effective parameter updates [37]. Parallel tempering (i.e., running a sequence of interacting Markov chains in which the likelihood functions are successively relaxed) is applied to improve chain mixing within dimensions, and to increase the acceptance rate of jumps between dimensions [16, 36].

Given the experiment geometry, data prediction requires the computation of spherical-wave (full-wave) reflection coefficients, which is carried out using plane-wave decomposition in the Sommerfeld integral [10, 11]. In this chapter, the estimated model consists of homogeneous layers (over a semi-infinite halfspace), with each layer characterized by VGS [24–26] parameters: porosity, grain-to-grain compressional modulus, material exponent, and compressional viscoelastic time constant. The underlying assumption of VGS theory is that unconsolidated marine sediments can be considered as viscous fluids containing sediment grains in contact [24,25]. VGS theory predicts frequency dependence similar to Biot's theory at low to intermediate frequencies, but the physics of dispersion differ. Grain-to-grain shearing and the viscous losses of the very thin pore fluid layer at the grain-to-grain (micro) contacts describe dispersion according to VGS theory, whereas only viscous losses associated with the movement of the pore fluid through the mineral structure explain dispersion according to Biot theory [24–27].

The remainder of this chapter is organized as follows: Section 3.2 describes the experiment and data collection (Section 3.2.1), and data processing (Section 3.2.2).

Section 3.3 presents the theory of the forward model involving VGS (Section 3.3.1) and spherical-wave reflection-coefficient calculations (Section 3.3.2), and the Bayesian trans-D inversion formulation (Section 3.3.3) including likelihood function (Section 3.3.4) and parallel tempering (Section 3.3.5). The inversion implementation and results are presented in Section 3.4. Finally, Section 3.5 summarizes and discusses this work.

3.2 Experiment and Data

This section describes the experiment geometry, data collection and data processing common to both the Shallow Water Acoustic Measurement Instrument (SWAMI) and Piston Core 52 (PC52) sites at the New England Mud Patch.

3.2.1 Experiment

The high-resolution, wide-angle seabed reflection data were collected in late March, 2017, during SCBEX at the New England Mud Patch. This region is characterized by a relatively smooth, flat seabed with pre-dominantly silt-sized particles. The survey geometry involved a ship-towed broadband Uniboom source and two bottom-moored omni-directional receivers. The source was mounted to a $\sim 1 \times 2$ m catamaran deployed roughly 30 m aft of the ship, towed at a depth of $\sim$0.4 m, and emitted a short pulse ($<$1 ms) with a broad bandwidth (0.1–10 kHz) every second. The acoustic data were recorded by the two receivers positioned at nominal elevations of 11 and 15 m, far enough above the seabed to prevent interference between the direct and bottom-reflected acoustic arrivals. The ship transited as slowly as practical (roughly 3 knots or 1.5 m/s) while navigating along a radial track with the track centre intended to be directly over the vertical array position. More precisely, the SWAMI site data were collected March 31, 2017, at 40.4614°N, $-$70.5753°W in $\sim$76 m of water, and the PC52 site data were collected on March 28, 2017, at 40.4838°N, $-$70.7469°W in $\sim$77 m of water. At both sites, conductivity-temperature-depth casts measured nearly isothermal water column sound-speed profiles around 1473 and 1470 m/s at the SWAMI and PC52 sites, respectively.

Two independent surveys of the New England Mud Patch were conducted in 2015 and 2016 in support of SCBEX [19]. In 2015, a dense ($\sim$250 m line spacing) chirp seismic reflection survey produced two-way-travel-times (TWTT) interpolated over the approximately-even grid of measurements. These TWTT can be used with

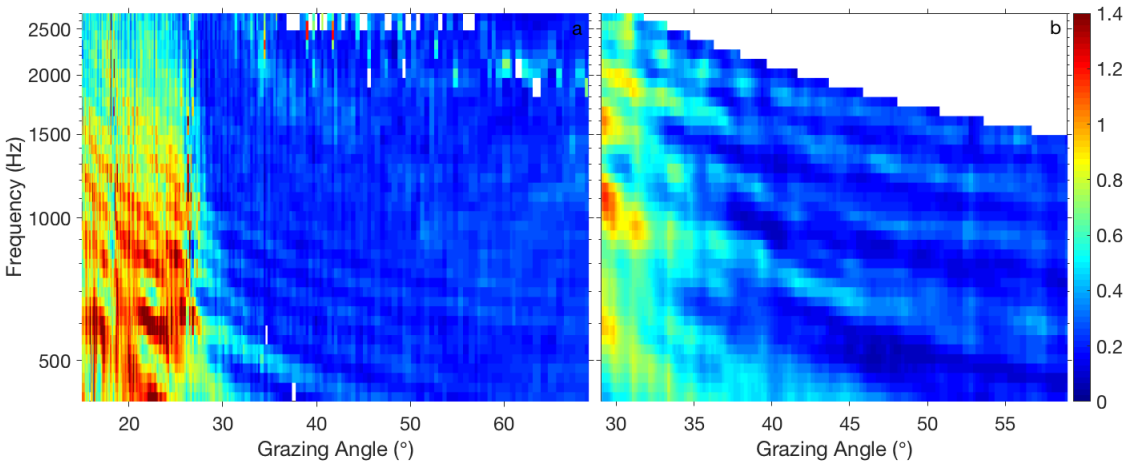

Figure 3.1: Seabed reflection-coefficient data averaged across frequency using $1/15^{\text{th}}$ octave bands, and angle averaged and interpolated over 0.75° evenly-spaced angular bins at the (a) SWAMI site and (b) PC52 site.

sediment velocities to estimate interface depths. The following year, a core survey, collected for engineering/geology purposes, characterized other sediment properties (e.g., density and porosity) that can be compared to inversion results. Note, the TWTT data for the PC52 site was not available at the time of this work.

3.2.2 Data Processing

First, the linearized ray-based inversion of acoustic travel-time data for high precision experiment geometry and uncertainties described in Chapter 2 was performed for both sites. The estimated high-precision experiment geometries were used in computing grazing angles along the survey tracks, with uncertainties computed using Monte Carlo methods. Subsequently, the reflection-coefficient data (as a function of grazing angle and frequency) were computed from time-windowed direct and bottom-reflected arrivals and corrected for experimental effects including source directivity, geometric spreading, and absorption in the water [21, 22]. The bottom response was time-windowed to ∼16 and 14 m depth below the seafloor at the SWAMI and PC52 sites, respectively.

The reflection-coefficient data inverted here were computed using acoustic time series from the shallow receiver at both sites. The reflection coefficients were frequency averaged over $1/15^{\text{th}}$ octave bands, and angle averaged and interpolated over 0.75° evenly-spaced angular bins. Moreover, reflection coefficients > 1.4 (outliers) were excluded. For the SWAMI site, a total of 46 reflection-coefficient data for grazing

angles between 25° and 60° at each of nine frequency bands selected from 400 to 1200 Hz are considered in this chapter. For the PC52 site, 42 data for grazing angles between 29° and 60° at each of nine frequency bands chosen between 400 to 1300 Hz are used here. The angular ranges were selected to remove high-noise levels and low information content in reflection-coefficient data at low- and high-grazing angles, respectively.

The reflection-coefficient data at all frequencies for both sites are shown in Fig. 3.1. The constructive/destructive interference from up- and down-going waves between the water-sediment interface and deeper interfaces causes the interference patterns shown in the figure. At the SWAMI site (Fig. 3.1(a)), the critical angle [2] is observed at approximately 27°, below which there is high (near unity) reflectivity.

3.3 Forward and Inverse Theory

This section provides an overview of the forward model involving VGS and spherical-wave reflection-coefficient calculations, and the Bayesian trans-D inversion method applied in this chapter.

3.3.1 Sediment Model: Viscous Grain-shearing

The VGS theory is based on the assumption that unconsolidated marine sediments can be considered as a viscous fluid containing sediment grains in contact [24,25]. The assumed bonding/loss mechanisms are due to grain-to-grain shearing (i.e., friction) and fluid flow around the grains in contact (i.e., viscosity). The VGS parameterization used here for geoacoustic inversion consists of a set of parameters which vary from layer to layer and another set of parameters which are taken to be layer/depth independent (i.e., a single value for all sediment layers) [10,28]. The layered parameters include porosity ϕ, grain-to-grain compressional modulus γ_p, material exponent n, and compressional viscoelastic time constant τ_p. The time constant is an important parameter as it governs the transition between the two bonding/loss mechanisms (i.e., viscous and frictional losses) which cause different attenuation-frequency dependencies. The depth-independent parameters include interstitial fluid density ρ_w and bulk modulus κ_w, and granular density ρ_g and modulus κ_g. These depth-independent parameters are reasonably well known and therefore constrained by uniform priors, representing uncertainties of the expected values to take these into account in the inversion [10, 28].

The bulk density ρ_0 and bulk modulus κ_0 of the sediment may be expressed in terms of the mean of the water and grain properties weighted by porosity, i.e., [24]

$$\rho_0 = \phi\rho_w + (1-\phi)\rho_g, \tag{3.1}$$

$$\frac{1}{\kappa_0} = \phi\frac{1}{\kappa_w} + (1-\phi)\frac{1}{\kappa_g}. \tag{3.2}$$

The compressional-wave velocity of an equivalent suspension is given by the Mallock-Wood approximation [12, 28]

$$c_0 = \sqrt{\frac{\kappa_0}{\rho_0}}. \tag{3.3}$$

The dimensionless grain coefficient χ is defined as [25]

$$\chi = \frac{\gamma_p + (4/3)\,\gamma_s}{\rho_0\, c_0^2}, \tag{3.4}$$

where γ_s is the grain-to-grain shear modulus. The sediment compressional-wave velocity and attenuation at angular frequency $\omega = 2\pi f$ (where f is frequency) are then [25, 26]

$$c_p = \frac{c_0}{\mathrm{Re}\left[1 + \chi(j\omega T)^n\left(1 + \frac{1}{j\omega\tau_p}\right)^{n-1}\right]^{-1/2}}, \tag{3.5}$$

$$\alpha_p = \frac{\omega}{c_0}\,\mathrm{Im}\left[1 + \chi(j\omega T)^n\left(1 + \frac{1}{j\omega\tau_p}\right)^{n-1}\right]^{-1/2}, \tag{3.6}$$

where Re and Im represent real and imaginary parts, respectively, $j = \sqrt{-1}$ is the imaginary unit, and $T = 1$ s is an arbitrary time introduced to avoid awkward units in the terms that are raised to a fractional power.

The VGS theory implemented here in fact follows a modified form of Buckingham's VGS(λ) theory [26]. The theories differ only when considering shear wave properties. In this work, the grain-to-grain shear modulus γ_s in (3.4) is not inferred but rather approximated by [26, 28]

$$\gamma_s = \frac{\gamma_{p0}}{10}\left[\frac{(1-\phi)\,u_g}{(1-\phi_0)\,u_{g0}}\right]^{2/3}, \tag{3.7}$$

where

$$\gamma_{p0} = \gamma_p\left[\frac{(1-\phi)\,u_g}{(1-\phi_0)\,u_{g0}}\right]^{-1/3}. \tag{3.8}$$

In (3.7) and (3.8), the terms $\phi_0 = 0.377$ and $u_{g0} = 10^{-3}$ are fixed, and the mean grain size u_g is given by

$$u_g = \frac{2\Delta\,(2B-1)}{1-B}, \tag{3.9}$$

where $\Delta = 10^{-6}$ represents an approximation to the mean roughness of the surface of the grains, and

$$B = \left(\frac{1-\phi}{1-\phi_{\min}}\right)^{1/3}, \tag{3.10}$$

where $\phi_{\min} = 0.37$ represents the minimum porosity in coarse-grained sands [24].

The VGS parameters and dispersion relationships given by (3.5) and (3.6) can be used to compute compressional-wave velocities and attenuations at various frequencies to investigate dispersion for each layer in the sediment model, as well as the parameters of a fluid model of the sediments.

3.3.2 Forward Modelling: Spherical-wave Reflection Coefficients

This section summarizes the reflection-coefficient forward model used in the inversion algorithm. Here, the forward model computes spherical-wave (full wave) reflection coefficients R_s as required due to the experiment geometry and source-frequency bandwidth [10,11,29,54]. Accordingly, predicted data for a geoacoustic model $\mathbf{m}$ are computed by scaling the acoustic pressure by the Green's function along the specular path (of length D) and accounting for the source beam-pattern S [54]

$$R_s(\theta, f, z_t, \mathbf{m}) = \frac{jkD}{\mathrm{e}^{jkD}\,S(\theta, f)} \int_0^{\pi/2-j\infty} S(\theta', f)\, J_0(k\,r\cos\theta')\, \mathrm{e}^{-jkz_t\sin\theta'} \times R_p(\theta', f, \mathbf{m}) \cos\theta'\, \mathrm{d}\theta', \tag{3.11}$$

where θ represents the specular reflection angle for a given offset, z_t represents the sum of the two distances from the source and the receiver to the seabed, k is the wavenumber, R_p represents the plane-wave reflection coefficient computed recursively, and J_0 is the zeroth-order Bessel function. The integral in (3.11) is solved numerically using Levin integration [11] and evaluated for each frequency and angle considered in the inversion. This computationally-intensive forward model is implemented massively in parallel using a compute unified device architecture on graphics processing units (GPUs), greatly reducing computation time [10,11].

3.3.3 Trans-dimensional Bayesian Formulation

The trans-D inversion formulation applied here is a generalization of the fixed-D problem that includes the number of model parameters as an unknown in the problem [33–35, 37]. In this chapter, the inversion samples probabilistically over an unknown number of sediment-layer interfaces and parameters of a zeroth- or first-order autoregressive error model. Consider $\mathbf{d}$ and $\mathbf{m}$ to be vectors of data and model parameters, respectively, and hyper-parameter k the unknown number of sediment interfaces. Assuming all of these to be random variables, they are related through Bayes' rule for a hierarchical model [33, 34]

$$P(k, \mathbf{m}_k|\mathbf{d}) = \frac{P(k)\, P(\mathbf{m}_k|k)\, P(\mathbf{d}|k, \mathbf{m}_k)}{\sum_{k' \in \mathcal{K}} \int_{\mathcal{M}_{k'}} P(k')\, P(\mathbf{m}'_{k'}|k')\, P(\mathbf{d}|k', \mathbf{m}'_{k'})\, \mathrm{d}\mathbf{m}'_{k'}}, \tag{3.12}$$

where $\mathcal{M}_k$ represents the M_k-dimensional parameter space defined for k and $\mathcal{K}$ is the set of possible values for k. In (3.12), $P(k)\, P(\mathbf{m}_k|k)$ is the prior probability of the state $(k, \mathbf{m}_k)$, and $P(\mathbf{d}|k, \mathbf{m}_k)$ is the conditional probability of $\mathbf{d}$ given $(k, \mathbf{m}_k)$, which is interpreted as the likelihood $\mathcal{L}(k, \mathbf{m}_k)$. $P(k, \mathbf{m}_k|\mathbf{d})$ is the PPD representing the total information about the model including both the data and prior information. This PPD is defined over the trans-D model space which represents the union of all fixed-D spaces specified by $\mathcal{K}$, i.e., $\cup_{k \in \mathcal{K}} \Big(\{k\} \times \mathbb{R}^{M_k} \Big)$. The denominator (normalization) in (3.12) represents the total evidence over all models specified by $\mathcal{K}$.

The trans-D PPD can be approximated by the numerical sampling method of rjMCMC, which transitions (or jumps) between system representations specified by k for models of dimension M_k while maintaining reversibility (detailed balanced) according to [33, 34]

$$P(k, \mathbf{m}_k|\mathbf{d})\, T(k', \mathbf{m}'_{k'}|k, \mathbf{m}_k) = P(k', \mathbf{m}'_{k'}|\mathbf{d})\, T(k, \mathbf{m}_k|k', \mathbf{m}'_{k'}). \tag{3.13}$$

In (3.13), $T(k', \mathbf{m}'_{k'}|k, \mathbf{m}_k)$ represents the transition probability to go from the current model $(k, \mathbf{m}_k)$ to a proposed (perturbed) model $(k', \mathbf{m}'_{k'})$. The proposal can be taken to be

$$T(k', \mathbf{m}'_{k'}|k, \mathbf{m}_k) = Q(k', \mathbf{m}'_{k'}|k, \mathbf{m}_k)\, A(k', \mathbf{m}'_{k'}|k, \mathbf{m}_k), \tag{3.14}$$

where Q is an arbitrary (but fixed) proposal probability density and A is the acceptance probability of a proposed transition. To satisfy reversibility, in rjMCMC, transitions are accepted with a probability given by the Metropolis-Hastings-Green

criterion [33, 34]

$$A(k', \mathbf{m}'_{k'}|k, \mathbf{m}_k) = \min\left[1, \frac{P(k', \mathbf{m}'_{k'})}{P(k, \mathbf{m}_k)} \frac{\mathcal{L}(k', \mathbf{m}'_{k'})}{\mathcal{L}(k, \mathbf{m}_k)} \frac{Q(k, \mathbf{m}_k|k', \mathbf{m}'_{k'})}{Q(k', \mathbf{m}'_{k'}|k, \mathbf{m}_k)} |\mathbf{J}|\right], \tag{3.15}$$

where $|\mathbf{J}|$ is the determinant of the Jacobian matrix ensuring proper matching of dimensions between $(k, \mathbf{m}_k)$ and $(k', \mathbf{m}'_{k'})$. The most commonly-applied formulation of rjMCMC adds and removes interfaces (referred to as birth and death steps, respectively) such that the determinant of $\mathbf{J}$ is unity [35, 55].

The birth-death rjMCMC algorithm for the depth-dependent seabed model in this chapter is based on adding or removing sub-bottom interfaces which define homogeneous layers. The parameters consist of k interface depths z_k above a (fixed) bounding depth z_b and geoacoustic parameters $g_i, i = 1, \ldots, G$ for each of the $k + 1$ layers (k finite layers over a semi-infinite halfspace). The bounding depth z_b is pre-selected such that the data are insensitive to variations below this depth. The priors for g_i are taken to be bounded uniform distributions over physically-realistic values; the prior for interface depths is uniform over $[0,\ z_b]$; and the prior for k is represented by a Poisson distribution, i.e., [56]

$$P(k) = \frac{\lambda^k e^{-\lambda}}{k!}, \tag{3.16}$$

where λ is a real (fixed) positive number and $P(k)$ represents the probability of k interfaces bounded between $[1,\ k_{\max}]$.

The Markov chain is constructed by one of three types of steps (chosen with equal probability) at each iteration: birth, death, or perturbation. A birth step proposes adding a layer by uniformly sampling a depth on $[0, z_b]$ and inserting an interface at that depth. The physical properties of the new layer are chosen from the prior. A death step proposes removing an interface chosen at random and setting the parameters of the resulting (thicker) layer to either those above or below the interface being removed. In a perturbation step, the model parameterization is unchanged but perturbations are proposed in a PC parameter space where the axes align with the dominant correlation directions (i.e., PC parameters are uncorrelated). To do so, the PC transformation and appropriate perturbation length scales are obtained by eigenvector decomposition of the unit-lag covariance matrix (i.e., covariance averaging over the differences between successive models along the Markov chain) [37]

$$\mathbf{C}_m^1 = \sum_{s=1}^{S-1} (\mathbf{m}_{s+1} - \mathbf{m}_s)(\mathbf{m}_{s+1} - \mathbf{m}_s)^T, \tag{3.17}$$

where S indicates the number of samples averaged over and $(\cdot)^T$ represents transpose. When a birth or death step results in a model with a value of k which has not been encountered previously, a linearized approximation to the model covariance matrix

$$\mathbf{C}_m = [\mathbf{A}^T \mathbf{C}_d^{-1} \mathbf{A} + \mathbf{C}_p^{-1}]^{-1}, \tag{3.18}$$

is computed at the current model $\mathbf{m}_s$ and applied initially. In (3.18), $\mathbf{A}$ is the sensitivity (Jacobian) matrix of partial derivatives evaluated at $\mathbf{m}_s$, $\mathbf{A}_{ij} = \partial d_i(\mathbf{m}_s)/\partial m_j$, and $\mathbf{C}_p$ is the prior model covariance matrix representing a Gaussian prior density designed to approximate the uniform bounded priors (i.e., prior bound widths of Δm_i are approximated by taking $\mathbf{C}_p$ to be a diagonal matrix with variances equal to those of uniform distributions, $\left(\Delta m_i\right)^2/12$). Subsequently, the initial estimate for the model covariance matrix (3.18) is updated with the unit-lag covariance matrix (3.17) estimated from MCMC sampling, with the proposal density updated periodically (typically at intervals of hundreds to thousands of MCMC moves), which represents a diminishing adaptation [37, 57].

The orthogonal transformation (rotation) between physical parameters $\mathbf{m}$ and PC parameters $\tilde{\mathbf{m}}$ is [23]

$$\tilde{\mathbf{m}} = \mathbf{U}^T \mathbf{m}, \qquad\qquad \mathbf{m} = \mathbf{U}\tilde{\mathbf{m}}, \tag{3.19}$$

where $\mathbf{U}$ is the column-eigenvector matrix of the model covariance matrix

$$\mathbf{C}_m = \mathbf{U}\,\mathbf{W}\,\mathbf{U}^T, \tag{3.20}$$

and $\mathbf{W} = \text{diag}[w_i]$ is the eigenvalue matrix, with w_i representing the variance projected along eigenvector $\mathbf{u}_i$ (i.e., the variance of PC parameter $\tilde{m}_i$). PC parameters are perturbed individually, with the perturbation for $\tilde{m}_i$ drawn from a Cauchy proposal distribution with scale factor w_i, and the perturbed models rotated back to physical space for likelihood evaluation. Thus, the PC decomposition provides both directions and length scales for effective parameter updates.

All proposed birth, death, and perturbation steps are accepted with probability given by the Metropolis-Hastings-Green criterion (3.15). The acceptance criterion is applied by drawing a random number ξ from a uniform distribution on [0, 1] and accepting the new model $(k', \mathbf{m}'_{k'})$ if $\xi < A(k', \mathbf{m}'_{k'}|k, \mathbf{m}_k)$ as computed from (3.15). If the proposed step is rejected another copy of the current model is included in the Markov chain. Given the use here of uniform priors, symmetric parameter proposal

distributions, and geoacoustic parameters proposed from the prior in birth steps, the acceptance probabilities in (3.15) simplify to the likelihood ratio [37]

$$A(k', \mathbf{m}'_{k'}|k, \mathbf{m}_k) = \min\left[1, \frac{\mathcal{L}(k', \mathbf{m}'_{k'})}{\mathcal{L}(k, \mathbf{m}_k)}\right], \tag{3.21}$$

for all steps.

3.3.4 Likelihood Function

The likelihood function $\mathcal{L}(\mathbf{m})$ requires specifying the statistical distribution of the data errors including both measurement and theory errors. In many cases, the data uncertainty distribution is not well known *a priori* and the lack of specific information suggests that a simple distribution (e.g., Gaussian) be assumed (supported by the Central Limit Theorem and maximum entropy [56]), with statistical parameters estimated from the data. Assuming Gaussian-distributed errors, the general form of the likelihood is [23]

$$\mathcal{L}(\mathbf{m}, \mathbf{C}_d) = \frac{1}{(2\pi)^{N/2}|\mathbf{C}_d|^{1/2}} \exp\left[-\frac{1}{2}\,\mathbf{r}(\mathbf{m})^T \mathbf{C}_d^{-1} \mathbf{r}(\mathbf{m})\right], \tag{3.22}$$

where $\mathbf{r}(\mathbf{m}) = \mathbf{d} - \mathbf{d}(\mathbf{m})$ are data residuals (i.e., difference between measured and predicted data for model $\mathbf{m}$). The data covariance matrix $\mathbf{C}_d$ is often unknown.

Here we consider a first-order autoregressive AR(1) data error model to characterize the residual covariance [15, 31, 32]. The AR(1) error model is equivalent to a Toeplitz covariance matrix with exponentially decreasing off-diagonal terms [58]. Assuming N_D subsets of the N data (e.g., N_D different frequencies for reflection-coefficient data), with N_i data, standard deviation σ_i, and AR(1) parameter a_i for the i^{th} subset, the likelihood becomes

$$\mathcal{L}(\mathbf{m}, \boldsymbol{\sigma}) = \frac{1}{(2\pi)^{N/2} \prod_{i=1}^{N_D} \sigma_i^{N_i}} \exp\left[-\sum_{i=1}^{N_D}\sum_{j=1}^{N_i} \frac{|\,\mathbf{r}_{ij}^{(t)}(\mathbf{m})|^2}{2\sigma_i^2}\right]. \tag{3.23}$$

For the AR(1) hierarchical model, $\mathbf{r}_{ij}^{(t)}(\mathbf{m})$ in (3.23) represents the total data residuals given by

$$\mathbf{r}_{ij}^{(t)}(\mathbf{m}, \mathbf{a}) = \begin{cases} d_{ij} - d_{ij}(\mathbf{m}), & j = 1, \\ d_{ij} - d_{ij}(\mathbf{m}) + a_i\Big[d_{i(j-1)} - d_{i(j-1)}(\mathbf{m})\Big], & j = 2, \ldots, N_i. \end{cases} \tag{3.24}$$

The total data residuals are assumed to be uncorrelated Gaussian distributed with standard deviations σ_i, assumptions that are checked *a posteriori* by considering the data residuals. For unknown standard deviations it is straightforward to sample (3.23) over σ_i using MCMC methods [37].

The AR(1) coefficients are sampled as unknowns on the interval $[-0.5, 0.99]$, accounting for the AR-estimate uncertainty in the model when required. AR(1) coefficients are defined mathematically on the interval ± 1, where negative values indicate anti-correlated errors. However, strongly anti-correlated errors are not generally found in natural processes and hence a cut-off at -0.5 is applied. Utilizing both trans-D sampling and hierarchical error modeling provides a rigorous and general inversion approach.

3.3.5 Parallel Tempering

A challenge in trans-D inversion is achieving a reasonable acceptance rate for dimension jumps and complete sampling of potentially multi-modal structure within fixed-D subspaces. An effective approach is parallel tempering [10, 16, 37] which applies a sequence of interacting Markov chains that sample the PPD at different tempering parameter values $0 < \beta \leq 1$ (β is the reciprocal of what is sometimes referred to as sampling temperature). The acceptance criterion (3.21) for birth, death, and perturbation moves is relaxed by raising the likelihood to the power β, [36, 37]

$$A(\mathbf{m}'|\mathbf{m}) = \min\left[1, \frac{\mathcal{L}^{\beta}(\mathbf{m}')}{\mathcal{L}^{\beta}(\mathbf{m})}\right], \tag{3.25}$$

(models $\mathbf{m}$ and $\mathbf{m}'$ may be of different dimensions, but as this does not affect parallel tempering the distinction is not made here to simplify notation). The low-β chains have an increased probability of accepting lower-likelihood models, providing a wide search of the parameter space and increasing the possibility of bridging isolated modes. Conversely, high-β chains provide efficient local sampling. Probabilistic interchange (swaps) between chains of different temperings ensures high-β chains can access all regions of the space. To define the swap acceptance probability, consider two Markov chains with temperings β_i and β_j and current models $\mathbf{m}_i$ and $\mathbf{m}_j$, respectively. For randomly-chosen chains, the proposal is symmetric and the acceptance probability

for going from the current joint state to the proposed (swap) state is [37]

$$A\big((\mathbf{m}_j,\beta_i),(\mathbf{m}_i,\beta_j)|(\mathbf{m}_i,\beta_i)(\mathbf{m}_j,\beta_j)\big)=\min\left[1,\left(\frac{\mathcal{L}(\mathbf{m}_i)}{\mathcal{L}(\mathbf{m}_j)}\right)^{(\beta_j-\beta_i)}\right]. \tag{3.26}$$

Since chains at $\beta < 1$ provide biased sampling of the PPD (i.e., sample from $P(\mathbf{m})\mathcal{L}^{\beta}(\mathbf{m})$), only the samples collected by the $\beta = 1$ chains(s) are retained. Although the computational expense increases linearly with the number of parallel-tempering chains, the rate of PPD convergence may substantially outweigh this factor for suitably chosen temperings [16, 37]. Also, this approach provides much greater assurance that the PPD has been properly explored in sampling.

Lastly, a tempering-dependent proposal is applied to match the tempered acceptance criterion for each Markov chain. In other words, the likelihood (3.22) is raised to the power β to become [37]

$$\mathcal{L}^{\beta}(\mathbf{m})\propto\exp\left[-\frac{1}{2}\,\mathbf{r}(\mathbf{m})^T\left(\frac{\mathbf{C}_d}{\beta}\right)^{-1}\mathbf{r}(\mathbf{m})\right], \tag{3.27}$$

which is equivalent to dividing the data covariance matrix by β. Subsequently, the starting covariance estimate used to initialize the PC proposal for tempering β is taken to be

$$\mathbf{C}_m(\beta)=\left[\mathbf{A}^T\left(\frac{\mathbf{C}_d}{\beta}\right)^{-1}\mathbf{A}+\mathbf{C}_p^{-1}\right]^{-1}. \tag{3.28}$$

After this initialization, the unit-lag covariance matrix $\mathbf{C}_m^1(\beta)$ is computed from the rjMCMC sampling with tempering β and used to replace the initial linearized approximation. This procedure takes advantage of both the parallel tempering and PC proposal schemes described above, and is computationally inexpensive.

3.4 Results

This section presents results of trans-D Bayesian inversion of seabed reflection-coefficient data for geoacoustic parameters and uncertainties for two sites at the New England Mud Patch. For both data sets, trans-D inversions are carried out in parallel on 19 central processing units (CPUs), i.e., one master (host) and 18 workers, with the workers accessing two GPUs in a staggered fashion to hide the communication overhead [59]. A total of 18 Markov chains (one chain per worker) are simulated with logarithmically-spaced tempering values β, including four $\beta = 1$

Table 3.1
Summary of prior parameter bounds for trans-D inversion.

Model parameter (Units)	Lower bound	Upper bound
Error model parameters		
Data standard deviation σ_i	0.03	0.10
Autoregressive coefficients a_i	-0.50	0.99
Depth-dependent model parameters		
Porosity ϕ	0.22	0.85
Grain-to-grain comp. modulus γ_p (Pa)	7.943×10^6	3.981×10^8
Material exponent n	0.0398	0.3981
Viscoelastic time constant τ_p (ms)	0.03	50
Depth-independent model parameters		
Fluid density ρ_w (g/cm^3)	1.024	1.028
Granular bulk modulus κ_g (Pa)	3.550×10^{10}	3.650×10^{10}
Granular density ρ_g (g/cm^3)	2.60	2.64
SWAMI fluid bulk modulus κ_w (Pa)	2.225×10^9	2.235×10^9
PC52 fluid bulk modulus κ_w (Pa)	2.215×10^9	2.225×10^9

chains (unbiased).

An adaptive tempering schedule based on swap acceptance rates is applied to the first 50,000 samples. The average swap acceptance rate is computed for every 5,000 samples (acceptance rates are only assessed between $\beta = 1$ and the adjacent chain). The tempering parameter values are updated if the average swap acceptance rate is less than 0.2 or greater than 0.6. The tempering adaptation occurs on the master and the updated tempering schedule is sent to all workers thereafter. The tempering parameter values are fixed after 50,000 samples, which is discarded as burn-in.

Predicted spherical-wave reflection coefficients are computed for all grazing angles considered for nine centre frequencies, with the data at each centre frequency representing a seven-point average over a bandwidth of 1/15 the centre frequency (in keeping with the way the measured reflection-coefficient data were processed).

Trans-D inversions are all initiated from a simple one-interface, layer-over-a-halfspace model. Bounded uniform priors are used for all model parameters with the bounds used in this chapter given in Table 3.1. The results presented here are from 100 hours of parallel-computing time and 10^5 samples at $\beta = 1$, after chain thinning and removing the first $\sim 5 \times 10^4$ samples from the start of the chains as burn-in. Chain thinning is applied by only saving every 30^{th} sample of the $\beta = 1$ chains for inference; i.e., the number of samples presented represents 1/30 of the total samples accepted by the algorithm. Convergence of the inversions was assessed by comparing

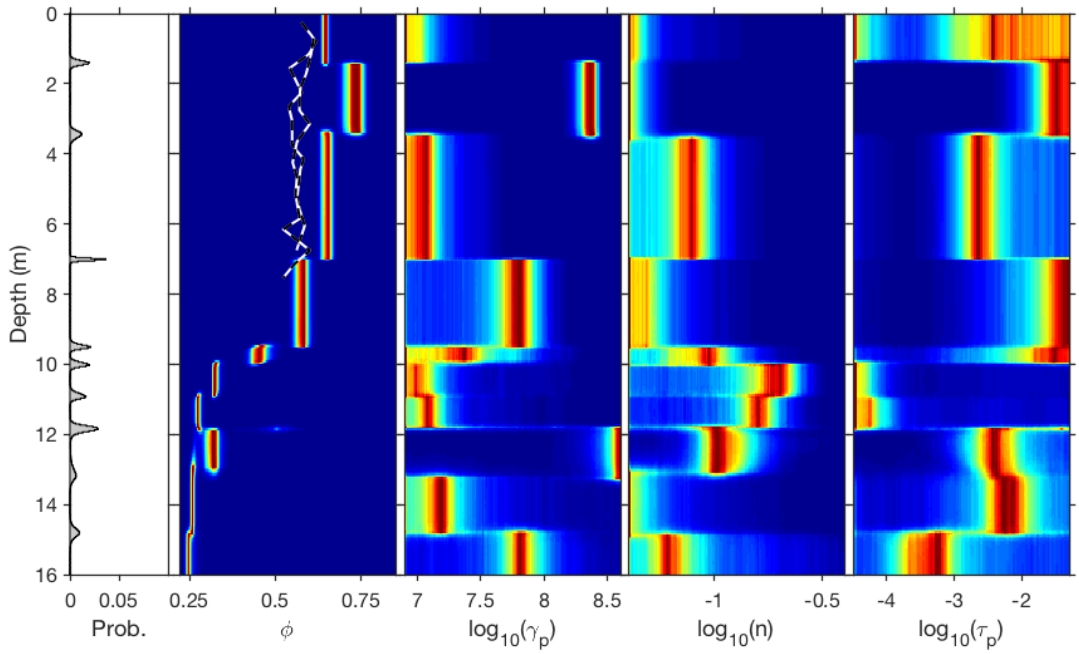

Figure 3.2: Trans-D marginal posterior probability profiles for interface depths and VGS parameters with plot boundaries representing prior bounds at the SWAMI site. The probabilities for the parameter profiles are normalized independently at each depth for display purposes. Porosity from two cores taken near the SWAMI site are plotted (dashed lines) on the porosity profile.

marginal posterior probability profiles computed for the first and second halves of the 10^5 samples. The profiles in all cases were virtually identical with no noticeable differences, indicating the PPD ceased to change significantly and convergence was achieved.

SWAMI Site

Two inversions with different priors on the number of interfaces k were considered at the SWAMI site. The first applied a prior on k characterized by a Poisson distribution (3.16) with $\lambda = 3$ as well as a uniform bounded prior on $[1, k_{\max}]$ with $k_{\max} = 20$. The second applied a uniform bounded prior with $k_{\max} = 6$ but no Poisson prior distribution. The results from the Poisson prior and wide bounds on k are presented first.

The inversion results for the VGS model parameters are shown in Fig. 3.2 and Fig. 3.3. The estimated depth-dependent parameters are illustrated in terms of marginal posterior probability profiles in Fig. 3.2, where warmer colours indicate

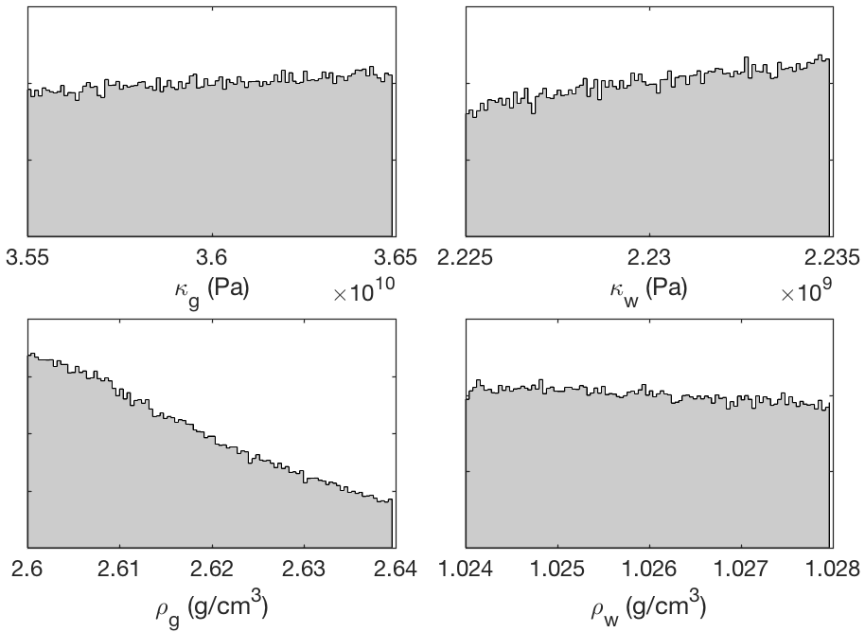

Figure 3.3: Marginal posterior probabilities for VGS depth-independent parameters with plot boundaries representing prior bounds at the SWAMI site.

regions of higher probability. Porosity ϕ is well resolved with comparatively smaller uncertainties (relative to its prior bounds) than the other parameters. The porosity profile indicates three general regions: (1) an upper region with a slow rate of general decrease in ϕ down to a depth of $\sim$9.5 m, (2) a steeper transition to smaller ϕ values from 9.5–12 m, and (3) a slow rate of general decrease in porosity below 12 m. A summary of mean porosities and 95% highest-probability density credibility intervals (CI) is given in Table 3.2 for selected depths. The grain-to-grain compressional modulus γ_p, material exponent n and compressional viscoelastic time constant τ_p are reasonably well determined relative to their priors. The VGS profiles include two dubious layers extending from about 1.5–3.5 and 12–13 m depth. For these layers ϕ reverses its overall trend, and γ_p makes abrupt changes to very high values. These may represent unphysical layers, possibly caused by theory errors, and will be discussed later.

The porosity profile is compared to values obtained from two piston cores taken near the SWAMI site (PC17 and PC33). The two cores both show relatively uniform porosities of $\sim$0.57 over their 7 m length. The inversion results are also relatively uniform over this depth with a porosity of about 0.65, except for the potentially unphysical layer. The small differences between cores and profile may be due to the fact that the cores may not have captured the correct amount of water in the fine-

Table 3.2
Summary of mean parameters and 95% CI at selected depths for the SWAMI site.

	ϕ		c_p (m/s)		ρ_0 (g/cm^3)		α_p (dB/m/kHz)	
Depth (m)	Mean	CI	Mean	CI	Mean	CI	Mean	CI
0	0.64	[0.62, 0.65]	1454	[1444, 1454]	1.59	[1.57, 1.60]	0.018	[0.005, 0.059]
5	0.65	[0.63, 0.67]	1454	[1448, 1460]	1.58	[1.55, 1.62]	0.028	[0.008, 0.070]
8.5	0.58	[0.55, 0.60]	1491	[1481, 1500]	1.70	[1.66, 1.75]	0.039	[0.012, 0.110]
11.5	0.27	[0.26, 0.28]	1795	[1770, 1817]	2.18	[2.15, 2.20]	0.022	[0.005, 0.083]
16	0.25	[0.23, 0.27]	1856	[1833, 1873]	2.22	[2.19, 2.25]	0.086	[0.012, 0.340]

grained sediments (due to their high permeability) [60]. This potentially inaccurate measure of water content can affect the calculations of the core porosity and density data presented here.

The marginal probabilities of the depth-independent parameters shown in Fig. 3.3, i.e., interstitial fluid density ρ_w and bulk modulus κ_w, and granular density ρ_g and modulus κ_g, are essentially flat over prior bounds for all four parameters, indicating the data have little ability to resolve these model parameters.

The parameters of a fluid model of the sediments, density ρ_0, compressional-wave velocity c_p, and attenuation α_p, can be computed from the VGS parameters using (3.1), (3.5), and (3.6), respectively. Marginal posterior probability profiles for the fluid parameters and interface depths at a frequency of 400 Hz are shown in Fig. 3.4. The same general depth regions are evident: (1) an upper region with a slow rate of general increase in c_p and ρ_0 down to a depth of $\sim$9.5 m, (2) a steeper transition to higher c_p and ρ_0 values from 9.5–12 m, and (3) a slow rate of general increase of these parameters below 12 m. The compressional-wave attenuation profile is relatively uniform with somewhat wider uncertainties compared to compressional-wave velocity and density. The potentially unphysical layers mentioned above manifest themselves as an anomalous high-velocity/low-density/high-attenuation layer from about 1.5–3.5 m depth and a low-density/high-attenuation layer from roughly 12–13 m depth. A summary of mean parameters and 95% CI at selected depths is included in Table 3.2.

The velocities in the upper region are generally low given the relatively-high density values and previously reported velocity/density relationships for unconsolidated marine sediments [3, 12, 61]. The density in the upper 7 m region is reasonably consistent with the values obtained from the cores (except for the potentially unphysical layer). The relatively low, water-like velocities and low attenuations suggest the upper region is acoustically transparent which is supported by the critical angle shown in Fig. 3.1. The critical angle indicates that waves transited the upper region with little reflection or attenuation loss to encounter a deeper sediment layer with a velocity

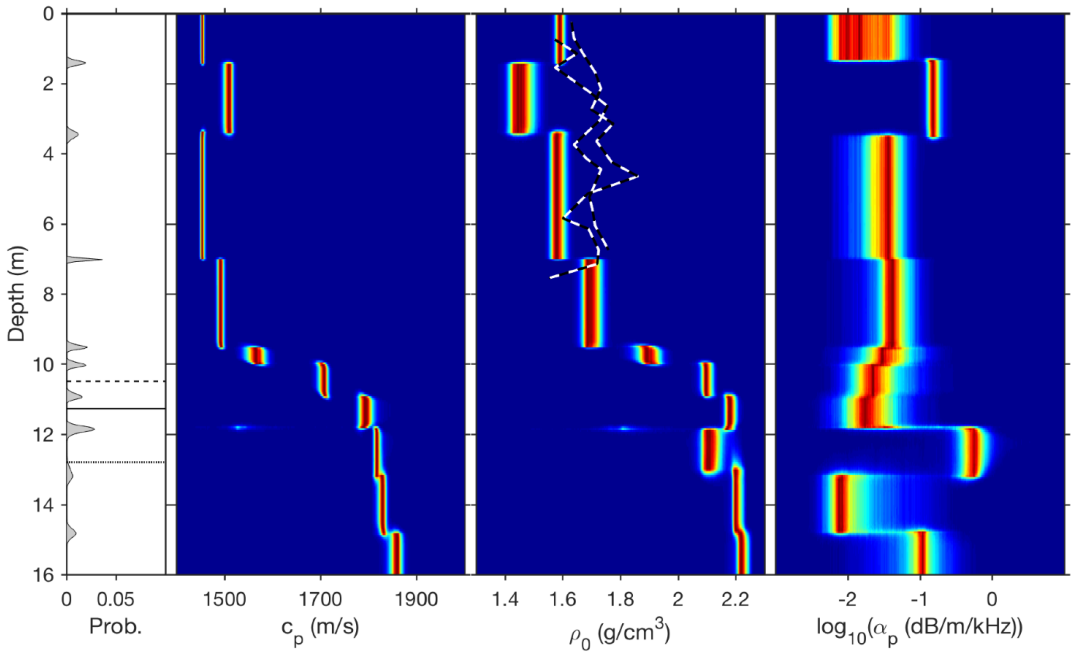

Figure 3.4: Trans-D marginal posterior probability profiles at 400 Hz for interface depths and fluid model parameters at the SWAMI site. The probabilities for the geoacoustic parameter profiles are normalized independently at each depth for display purposes. Interface estimates from the chirp seismic reflection survey are plotted over the interface marginal probability densities and densities from core data are plotted (dashed lines) over the geoacoustic parameter profile. In the interface depth marginal probability density plot, the upper (dashed) line represents the mud base, the middle (solid) line represents the sand base, and the lower (dotted) line represents the deep sand base interface estimates from TWTT data.

faster than that in the overlying region.

The geoacoustic and porosity profiles are indicative of a thick (∼9.5 m) region of fine-grained sediments (such as mud) over a deeper region of coarse-grained sediments (sand). Although the trans-D formulation estimates properties of discrete homogenous layers, the geoacoustic and VGS profiles may represent a transition between sediment types involving a gradient over which the properties change smoothly with depth. This transition region estimated by trans-D inversion agrees with chirp-seismic reflection horizon estimates (computed from harmonic-mean velocities and TWTT) included in Fig. 3.4. The TWTT reflection horizons (from shallowest to deepest) are the mud base, sand base and deep sand base. The mud base and sand base horizons are in agreement with the transition region estimated by trans-D inversion of about 9.5–12 m depth.

Fig. 3.5 shows compressional-wave velocity and attenuation as a function of fre-

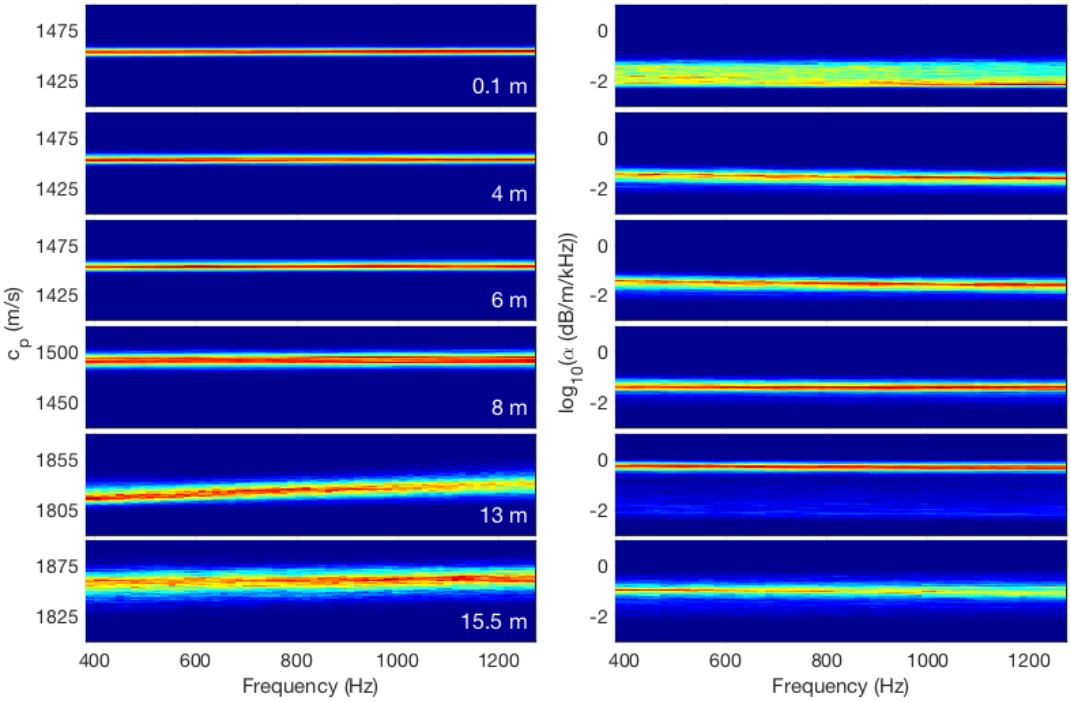

Figure 3.5: Dispersion-curve marginal probability distributions for selected (indicated) depths at the SWAMI site.

quency across the band of the measurement frequencies at depths of interest (indicated on the velocity plots). The compressional-wave velocities appear to be essentially unchanged across frequency at all depths, indicating little evidence of dispersion across the frequency band considered. The compressional-wave attenuation plotted as $\log_{10}(\alpha_p)$ is nearly constant over 400–1200 Hz at various depths, suggesting a first power dependence f^1 of attenuation on frequency in the fine-grained/cohesive sediments.

The sampling history and distribution of the number of interfaces k and likelihood values as a function of sample are shown in Fig. 3.6. The sampling history is consistent with stationary sampling (randomly distributed with no systematic change over a large number of samples). The k-distribution has uncertainty in number of interfaces between 6 and 14, with a peak at $k = 10$ well within the prior bounds.

The fit to the data achieved in the inversion is illustrated in Fig. 3.7 by comparing measured and predicted reflection coefficients as well as plotting marginal probability densities for standard deviations at each frequency. The measured reflection coefficients (crosses) are compared to predicted reflection coefficients (red dots) for a large ensemble of models drawn randomly from the PPD. The predictions fit the data well

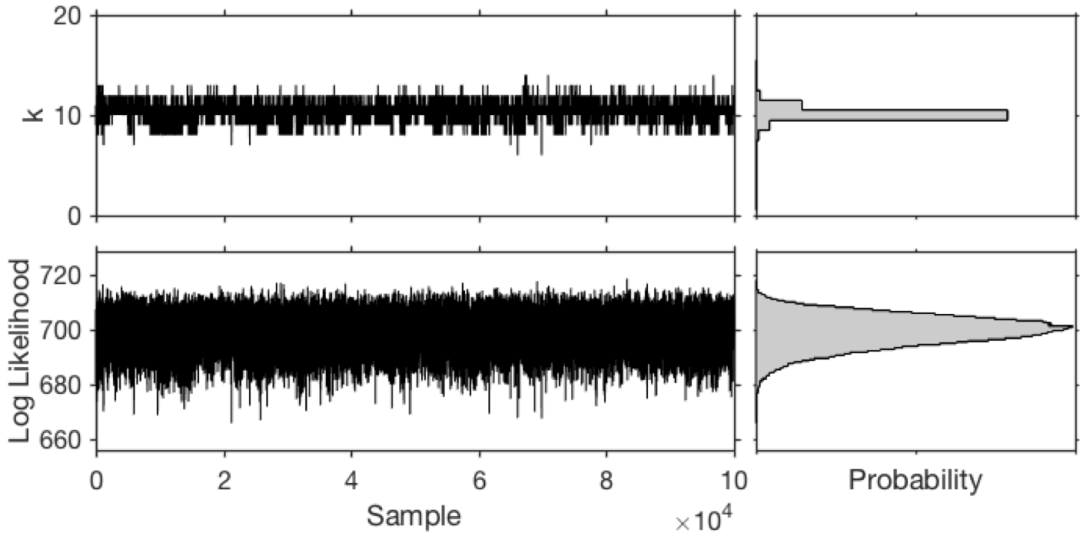

Figure 3.6: Sampling history and distribution of the number of interfaces k and likelihood values at the SWAMI site. The prior for k is a Poisson distribution with $\lambda = 3$ and a uniform bounded prior $[1, k_{\max}]$ with $k_{\max} = 20$.

across all angles and frequencies with the exception of a small number of outliers (particularly for high reflection coefficients). The estimated standard deviations at each frequency are generally small, between 0.04 and 0.06.

The order (zeroth or first) of the AR process and the distributions of the AR(1) coefficients are shown in Fig. 3.8. Five of the nine frequency bands favoured AR(1) error models (i.e., correlated errors) while one band was strongly AR(0), and three were seemingly undetermined. These marginals indicate that the data at some frequencies (particularly the lowest three frequencies) contain correlated errors. The AR(1) coefficient values are usually between 0–0.5.

The assumption of Gaussian-distributed residual errors with correlations described by a zeroth- or first-order autoregressive process is considered in Fig. 3.9. Histograms for the ensemble average of the total residual error (3.24) at each frequency are compared to Gaussian distributions in the upper two rows of this figure. The residuals at all frequencies appear unimodal, symmetric about zero, and generally Gaussian distributed with a small number of outliers (as far as four standard deviations). The narrow-peaked residual autocorrelation functions at each frequency (shown in the lower two rows of the figure) indicate the residuals at all frequencies are largely uncorrelated (when covariance is taken into account through the trans-D AR process). The ensemble residual analysis generally supports the initial assumptions about the residuals.

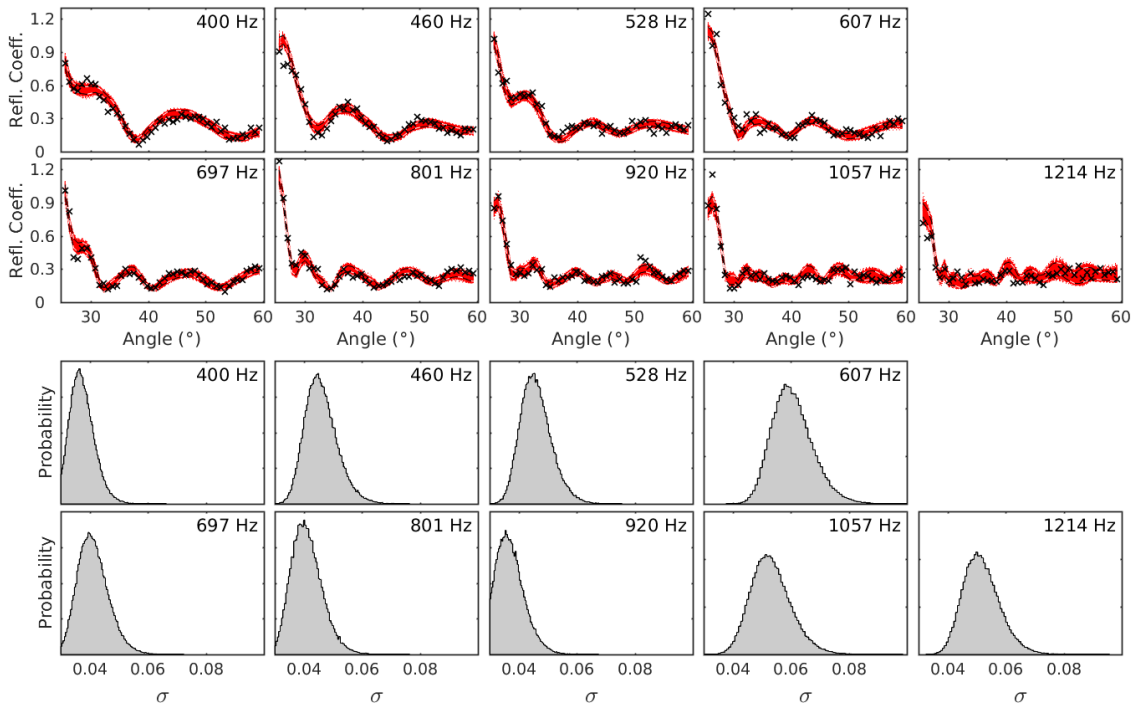

Figure 3.7: Fit to the data achieved at the SWAMI site. The upper two rows compare observed reflection-coefficient data (crosses) and predicted data for an ensemble of models (red dots) at each frequency. The lower two rows show marginal probability densities for the data standard deviations sampled explicitly in the inversion. The standard deviation plot bounds indicate the uniform prior bounds implemented in the inversion.

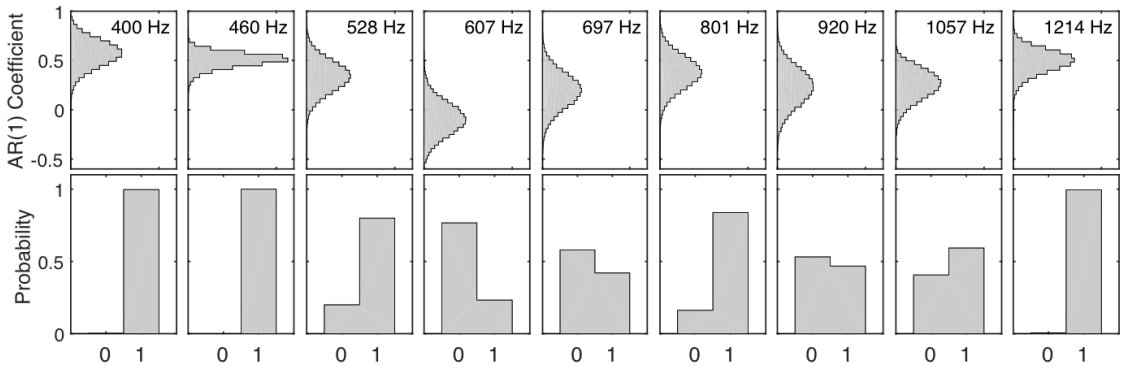

Figure 3.8: Autoregressive error model at the SWAMI site. The upper row shows marginal densities for the autoregressive coefficients. The lower row shows the probabilities of having an AR(0) or AR(1) error model (indicated by 0 and 1, respectively) as determined by the trans-D sampling algorithm.

A second trans-D inversion of the SWAMI data was carried out. In this inversion, a uniform bounded prior on the interval [1, 6] is applied for the number of interfaces k. This was carried out because the profiles in Fig. 3.2 and Fig. 3.4 show two layers at $\sim$1.5–3.5 and 12–13 m depth with properties that may be unphysical and are likely due to theory errors that are not properly taken into account. Theory errors can occur due to approximations and/or assumptions made in the forward problem (e.g., interface roughness and non-horizontally stratified sub-bottom layers) [62]. To address these possibly unphysical layers, the number of interfaces resolved by the data was estimated by considering the Bayesian information criterion (BIC) defined [63]

$$\mathrm{BIC}(k) = -2\log_e \mathcal{L}(k, \mathbf{m}_k^{\mathrm{ML}}) + k\,G\log_e N, \tag{3.29}$$

where $\mathbf{m}_k^{\mathrm{ML}}$ represents the maximum-likelihood model, G is the number of parameters per layer, and N is the total number of data (layer-independent parameters are not counted here for convenience). The first term on the right side of (3.29) favours high-likelihood models but is balanced by the second term which penalizes unjustified free parameters (e.g., too many interfaces). The number of interfaces resolved by the data estimated by minimizing the BIC was six. The BIC represents a point approximation of Bayesian evidence and is not a definitive approach to estimating the number of parameters for nonlinear inverse problems. Nonetheless, it provides a basis for considering simpler models to address the potentially unphysical layers.

The marginal posterior probability profiles for the VGS and fluid model parameters at 400 Hz obtained with a uniform bounded prior distribution for k between

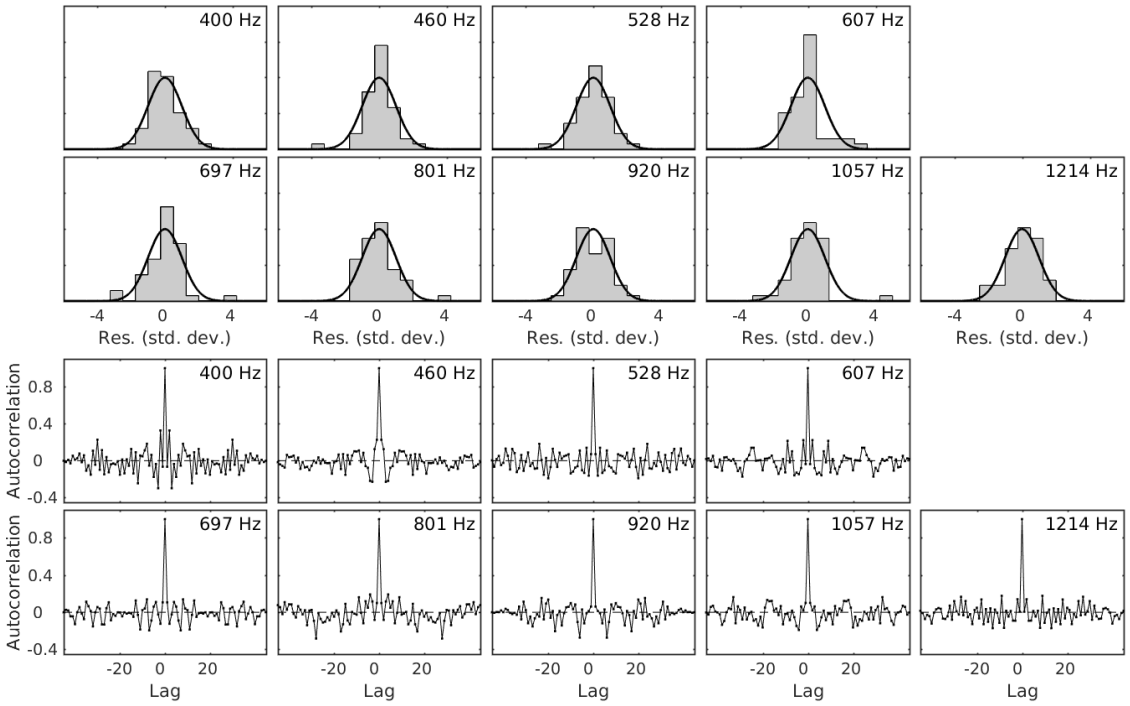

Figure 3.9: Ensemble residual analysis at the SWAMI site. The upper two rows show histograms of total data residuals compared to Gaussian distributions. The lower two rows show residual autocorrelation functions.

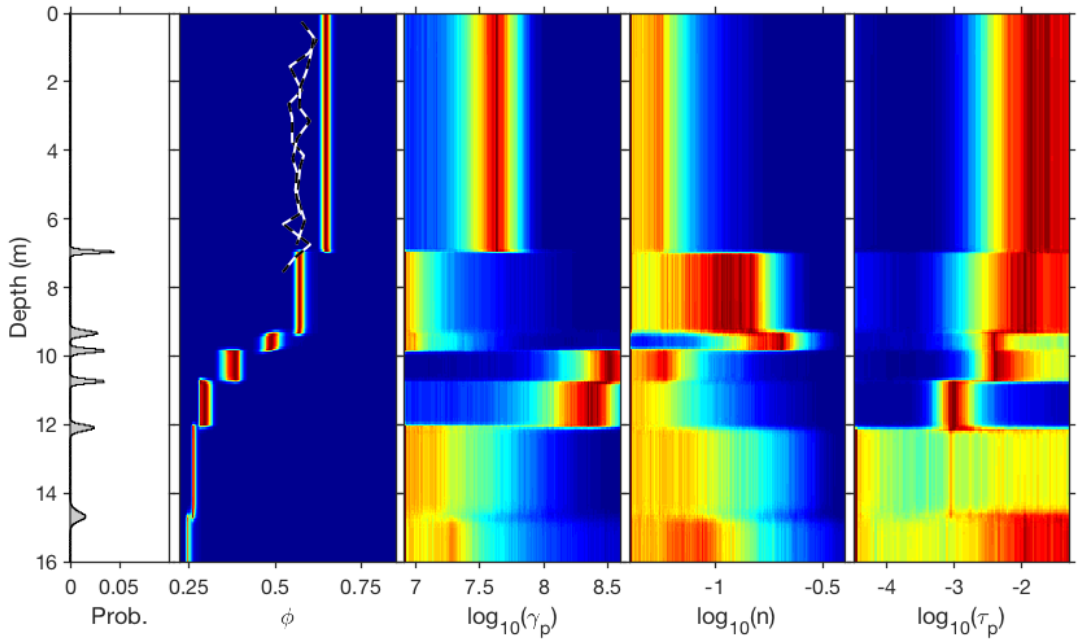

Figure 3.10: Marginal posterior probability profiles for VGS depth-dependent parameters with a uniform bounded prior (only) on k at the SWAMI site.

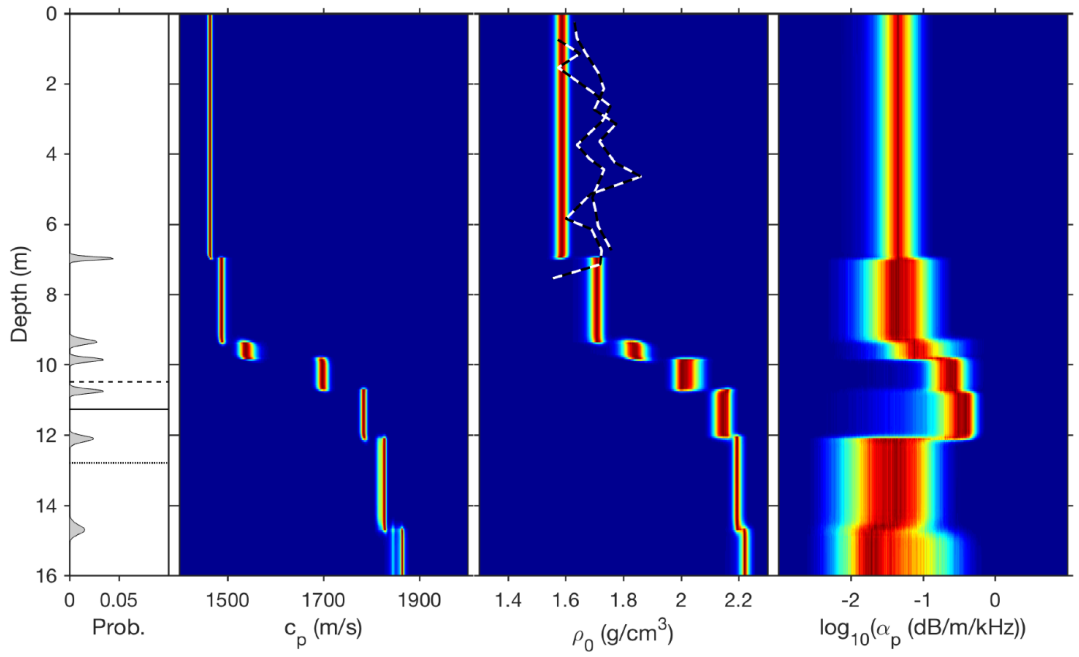

Figure 3.11: Marginal posterior probability profiles at 400 Hz for compressional velocity, density and log-attenuation as a function of depth in the sediment with a uniform bounded prior (only) on k at the SWAMI site.

[1, 6] are illustrated in Fig. 3.10 and Fig. 3.11, respectivey. The profiles display the same major features (with slightly wider uncertainties) as obtained with the Poisson prior distribution on k without the potentially unphysical structure shown in Fig. 3.4. The dispersion-curve marginal probability distributions are nearly identical to those from the initial inversion but with slightly wider uncertainties (not shown). Further, the fit to the data, AR(1) error model coefficients, and standard deviations for this inversion are very similar to those obtained with the Poisson prior for k. These results highlight the nonunique nature of geoacoustic inverse problems. This simpler model is presented as an alternate representation of the seabed that may be preferred in practice.

PC52 Site

As for the SWAMI site, two inversions with different k priors were considered for the PC52 site. The first applied a prior characterized by a Poisson distribution with $\lambda = 3$ together with a uniform bounded prior on $[1, k_{\max}]$ with $k_{\max} = 20$. The second applied a uniform bounded prior on $[1, k_{\max}]$ with $k_{\max} = 5$ but no Poisson prior distribution, where $k_{\max}$ was estimated using the BIC. The results from the Poisson prior and wide bounds on k are presented first.

The inversion results for the VGS model parameters and interface depths in terms of marginal posterior probability profiles are shown in Fig. 3.12. The porosity ϕ profile suggests four general regions: (1) an upper region with a slow rate of decrease in ϕ down to a depth of $\sim$2 m, (2) a steeper transition to smaller ϕ values between 2–3 m, (3) a generally uniform region (or slight decrease) in ϕ between 3–11 m, and (4) a region of highly-variable porosity below $\sim$11 m, which may be unphysical. A summary of mean porosities and 95% CI at selected depths is given in Table 3.3. The grain-to-grain compressional modulus γ_p, material exponent n and compressional viscoelastic time constant τ_p are reasonably well determined relative to their priors, but are highly variable with depth.

The porosity profile is compared to values obtained from a core (PC52) taken at the site. The trend of the core porosity agrees closely with the inversion results with differences in values that may be caused by inaccurate water-content measures. The upper region at the PC52 site has a comparatively higher porosity than at the SWAMI site, suggesting a higher content of silt- and/or clay-sized particles at the PC52 site [6, 64]. The marginal probabilities of the depth-independent parameters (not shown), are essentially flat over prior bounds for all four parameters.

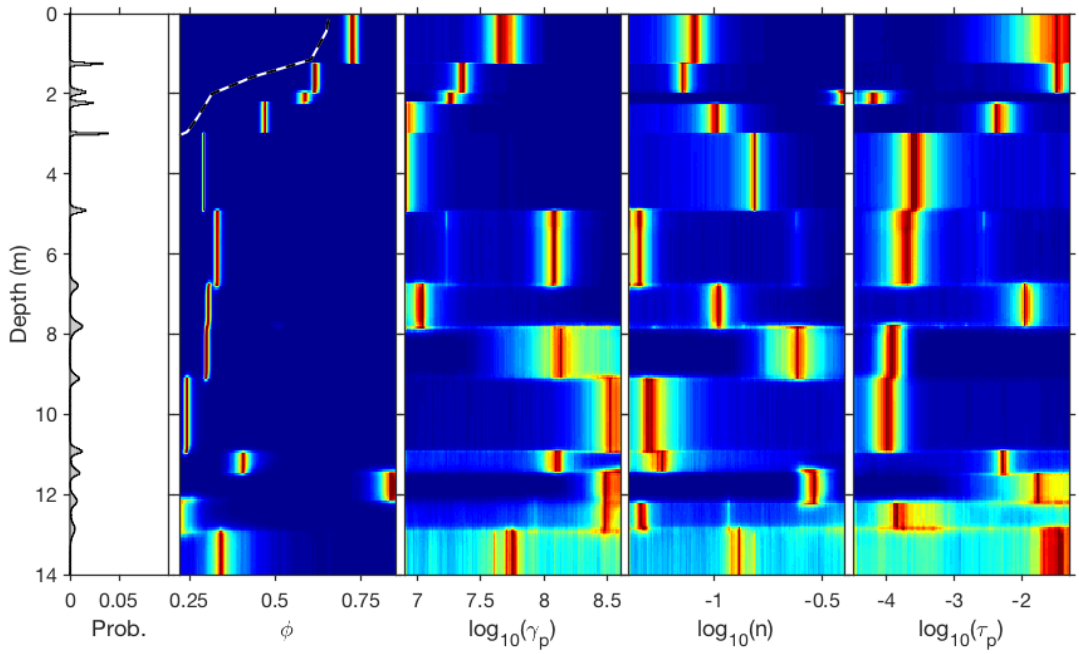

Figure 3.12: Trans-D marginal posterior probability profiles for interface depth and VGS parameters with plot boundaries representing prior bounds at the PC52 site. The probabilities for the parameter profiles are normalized independently at each depth for display purposes. Porosity from a core taken at the site is plotted (dashed line) over the porosity marginal profile.

Marginal posterior probability profiles for the fluid parameters at a frequency of 400 Hz are shown in Fig. 3.13. The same general depth regions are evident: (1) an upper region with a slow rate of increase in velocity c_p and density ρ_0 down to a depth of ∼2 m, (2) a steeper transition to higher c_p and ρ_0 values between 2–3 m, (3) a generally uniform region (or slight increase) in these parameters between 3–11 m, and (4) a region of highly variable properties below ∼11 m. The compressional-wave attenuation α_p profile varies considerably with depth but seems to be centered about approximately 0.1 dB/m/kHz. A summary of mean parameters and 95% CI at selected depths is given in Table 3.3.

The density in the upper region is reasonably consistent with the values obtained from the core (to ∼3 m depth) with excellent agreement in near-surface values. The decrease in core densities below roughly 3 m depth may be due to core decompression which can occur in the bottom section of the core. The overall geoacoustic and porosity profiles are indicative of a thin (∼2 m) region of fine-grained sediments (such as mud) over a deeper region of coarse-grained sediments (sand).

The PC52 and SWAMI sites have very similar near-surface compressional-wave ve-

Table 3.3
Summary of mean parameters and 95% CI at selected depths for the PC52 site.

	ϕ		c_p (m/s)		ρ_0 (g/cm^3)		α_p (dB/m/kHz)	
Depth (m)	Mean	CI	Mean	CI	Mean	CI	Mean	CI
0	0.72	[0.69, 0.74]	1451	[1434, 1460]	1.47	[1.42, 1.50]	0.077	[0.028, 0.180]
1.5	0.62	[0.60, 0.64]	1464	[1456, 1473]	1.64	[1.60, 1.66]	0.031	[0.012, 0.110]
2.5	0.47	[0.45, 0.48]	1543	[1528, 1550]	1.87	[1.83, 1.89]	0.022	[0.008, 0.060]
4.0	0.29	[0.28, 0.30]	1759	[1751, 1767]	2.15	[2.13, 2.18]	0.034	[0.008, 0.140]
8.5	0.30	[0.29, 0.31]	1751	[1735, 1765]	2.14	[2.11, 2.17]	0.820	[0.450, 1.200]
10	0.24	[0.23, 0.27]	1858	[1826, 1887]	2.23	[2.18, 2.26]	0.190	[0.052, 0.550]

locities of 1451 and 1454 m/s, respectively (see Tables 3.2 and 3.3) and sound-velocity ratios (between near-surface sediment compressional-wave velocity and bottom-water velocity) < 1. Although there are small differences in near-surface density values between the two sites (1.47 and 1.59 g/cm^3 at the PC52 and SWAMI site, respectively), both sites show good agreement with core density data.

Fig. 3.14 shows compressional-wave velocity and attenuation as a function of frequency at selected depths. There is little evidence of dispersion to ∼7.5 m depth across the frequency band considered (i.e., velocities are essentially unchanged across frequency) and $\log_{10}(\alpha_p)$ from 400–1300 Hz is nearly constant at various depths, indi-

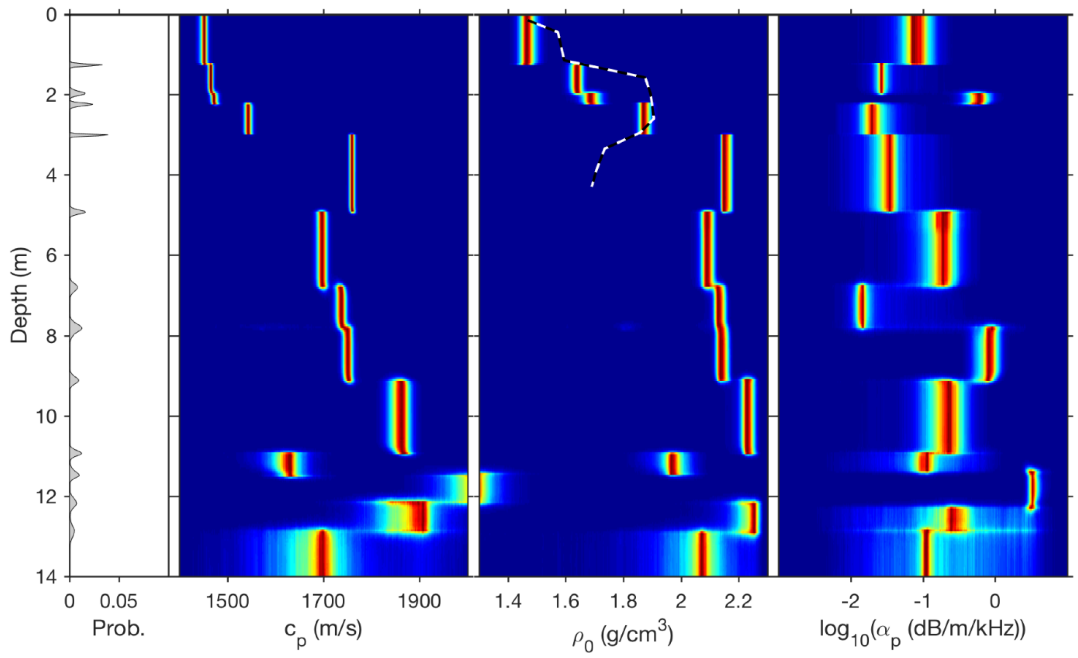

Figure 3.13: Trans-D marginal posterior probability profiles at 400 Hz for estimated compressional velocity, density and attenuation at the PC52 site. Densities from core data are plotted (dashed lines) over the geoacoustic parameter profile.

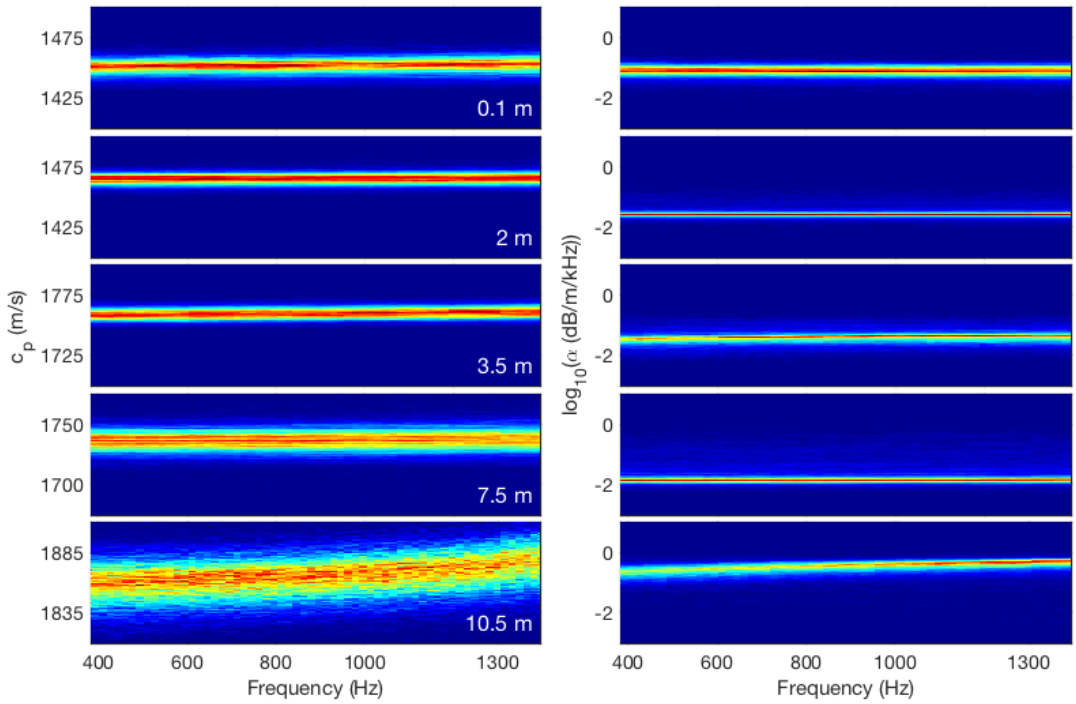

Figure 3.14: Dispersion-curve marginal probability distributions for selected (indicated) depths at the PC52 site.

cating a linear attenuation-frequency dependence. At 10.5 m depth there appears to be an increase in c_p with frequency, although it is not clear that this exceeds uncertainties. Likewise, $\log_{10}(\alpha_p)$ appears to increase over frequency at a depth of about 10.5 m, suggesting a higher order frequency dependence.

The sampling history and distribution of the number of interfaces k and likelihood values of the sampled models at PC52 are shown in Fig. 3.15 and are consistent with stationary sampling. The k-distribution has uncertainty in number of interfaces between 7 and 18, with a peak at $k = 13$.

The fit to the data achieved in the inversion is illustrated in Fig. 3.16. The predicted reflection coefficients generally fit the measured data well across angles and frequencies, with the exception of 920 Hz where some of the structure of the measured reflection coefficients at low- and medium-grazing angles are not captured by the prediction ensemble. The estimated standard deviations at each frequency are generally small, between 0.04 and 0.05, with the exception of 920 Hz where the standard deviation is $\sim$0.07.

The order of the AR process and the distributions of the AR(1) coefficients are shown in Fig. 3.17. Six of the nine frequency bands favour AR(1) error models while

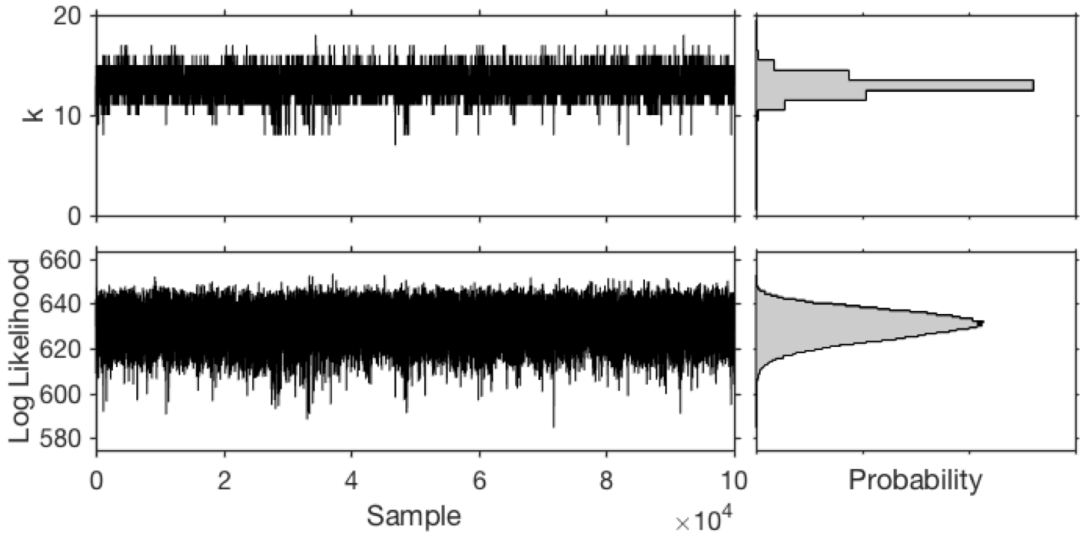

Figure 3.15: Sampling history and distribution of the number of interfaces k and log-likelihood values at the PC52 site. The prior for k is characterized by a Poisson distribution.

two bands are strongly AR(0), and one is seemingly undetermined, indicating that the data contain correlated errors at some but not all frequencies.

The assumptions about the residuals are examined by comparing histograms of the ensemble average of the total residual error to Gaussian distributions, and by examining residual autocorrelation functions, shown in Fig. 3.18. The residuals at all frequencies appear generally Gaussian distributed with very few outliers. The residual autocorrelation functions show narrow peaks at each frequency, suggesting uncorrelated total residuals.

A second trans-D inversion of the PC52 data was carried out due to the high variability in parameter estimates (particularly at depth) which suggests the trans-D inversion may have over-parametrized the model due to unaccounted for theory errors. In this inversion, a uniform bounded prior on the interval [1, 5] is applied for the number of interfaces k to constrain structure. The upper bound of this uniform prior was estimated using the BIC.

The marginal posterior probability profiles at 400 Hz for compressional-wave velocity, density and attenuation obtained with a uniform bounded k prior distribution are shown in Fig. 3.19. The profiles display four major regions: (1) a uniform low-velocity and density region to about 2 m depth, (2) a transition region to higher values in c_p and ρ_0 from ∼2–3 m, (3) a uniform region between roughly 3–11 m, and (4) a region of high variability below about 11 m. The profiles also show three dubious layers

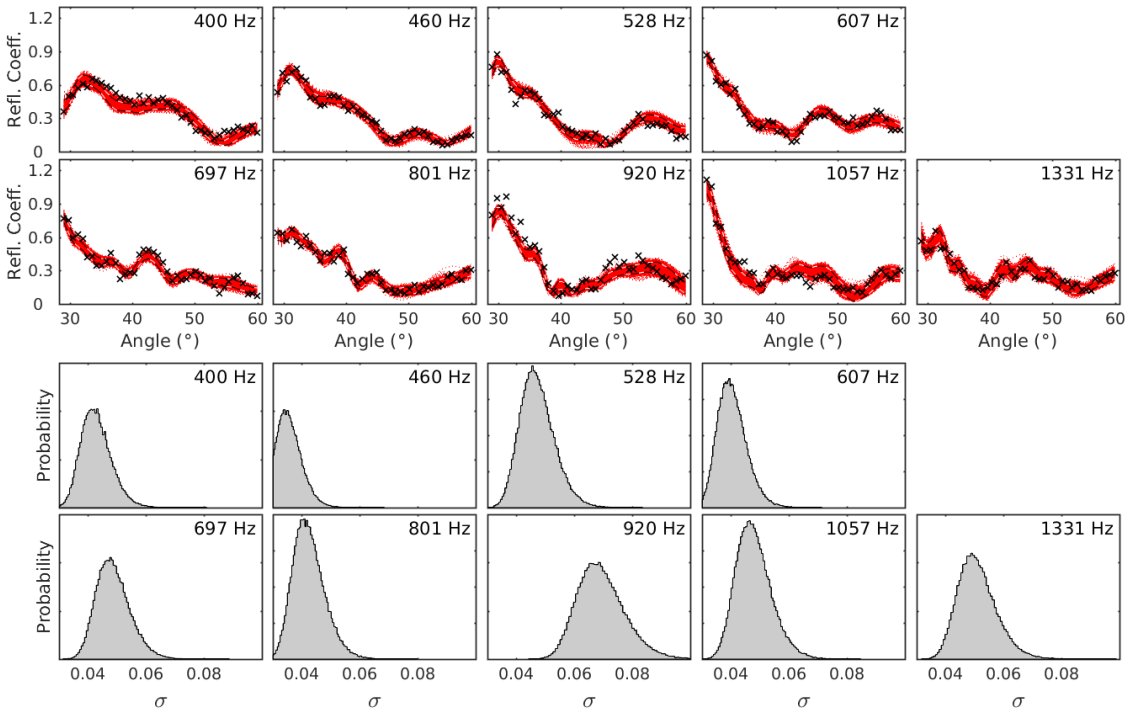

Figure 3.16: Fit to the data achieved at the PC52 site. The upper two rows compare observed reflection-coefficient data (crosses) and predicted ensembles (red dots) at each frequency. The lower two rows show marginal probability densities for the data standard deviations sampled explicitly in the inversion. The standard deviation plots bounds indicate the uniform prior bounds implemented in the inversion.

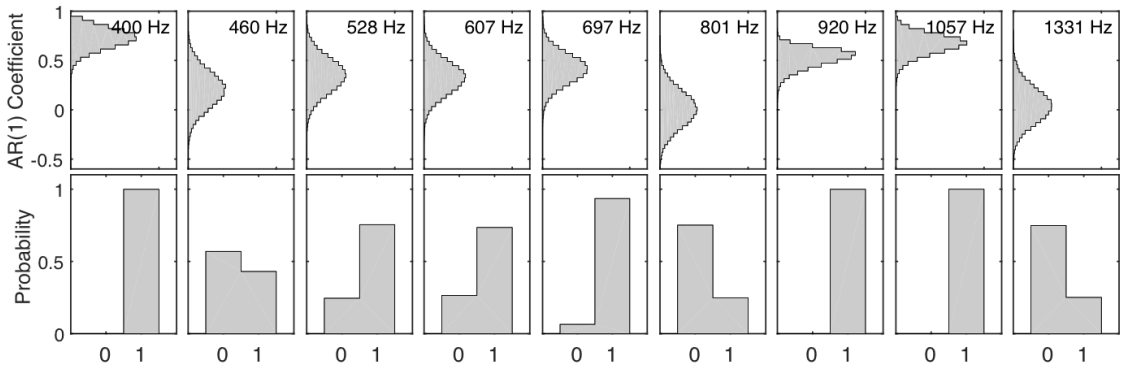

Figure 3.17: Autoregressive error model at the PC52 site. The upper row shows marginal densities for the autoregressive coefficients. The lower row shows the probabilities of having an AR(0) or AR(1) error model (indicated by 0 and 1, respectively) as determined by the trans-D sampling algorithm.

with potentially unphysical structure: a thin, low-density/high-attenuation layer at ∼2 m depth; a thin, low-velocity/low-density/high-attenuation layer at about 11 m depth; and a high-velocity/low-density/high-attenuation layer below ∼12 m. The density profile is in good agreement with the core data taken at the site with the exception of the thin layer at about 2 m depth. With the exception of this layer, the geoacoustic profiles are believed to be reliable to a depth of about 11 m.

The dispersion-curve marginal probability distributions, fit to the data, AR(1) error model coefficients, and standard deviations for this inversion (not shown) are very similar to those obtained with the Poisson prior and wide prior bounds for k.

3.5 Summary and Discussion

This chapter presented trans-D Bayesian geoaoustic inversion of seabed reflection-coefficient data for fine-grained/cohesive sediments for two sites of contrasting mud-layer thicknesses at the New England Mud Patch. The broadband wide-angle reflection-coefficient data were collected during SCBEX at the (thick-mud layer) SWAMI and (thin-mud layer) PC52 sites. The data are inverted to estimate VGS parameters of porosity, grain-to-grain compressional modulus, material exponent, and compressional viscoelastic time constant as a function of depth in the sediment. The geoacoustic parameters of a fluid model of the sediments are computed from VGS parameters, providing marginal probability profiles for compressional-wave velocity, density, and attenuation, and to investigate frequency-dependent behaviour of velocity and attenuation.

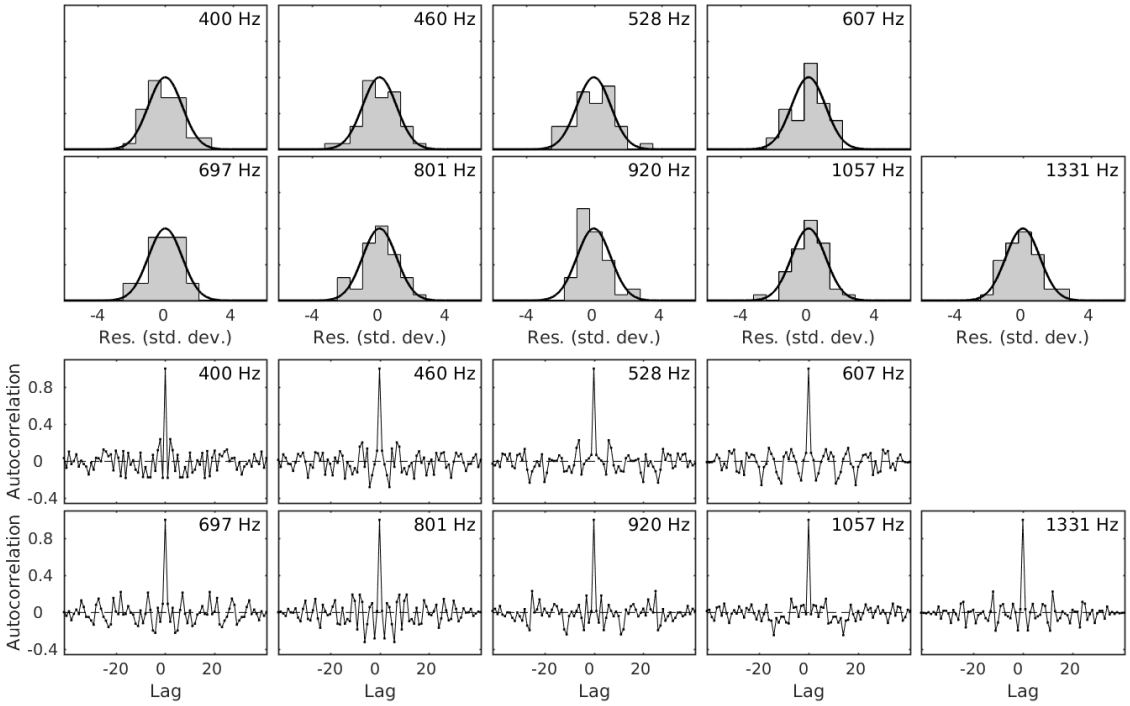

Figure 3.18: Ensemble residual analysis at the PC52 site. The upper two rows show histograms of total data residuals compared to Gaussian distributions. The lower two rows show residual autocorrelation functions.

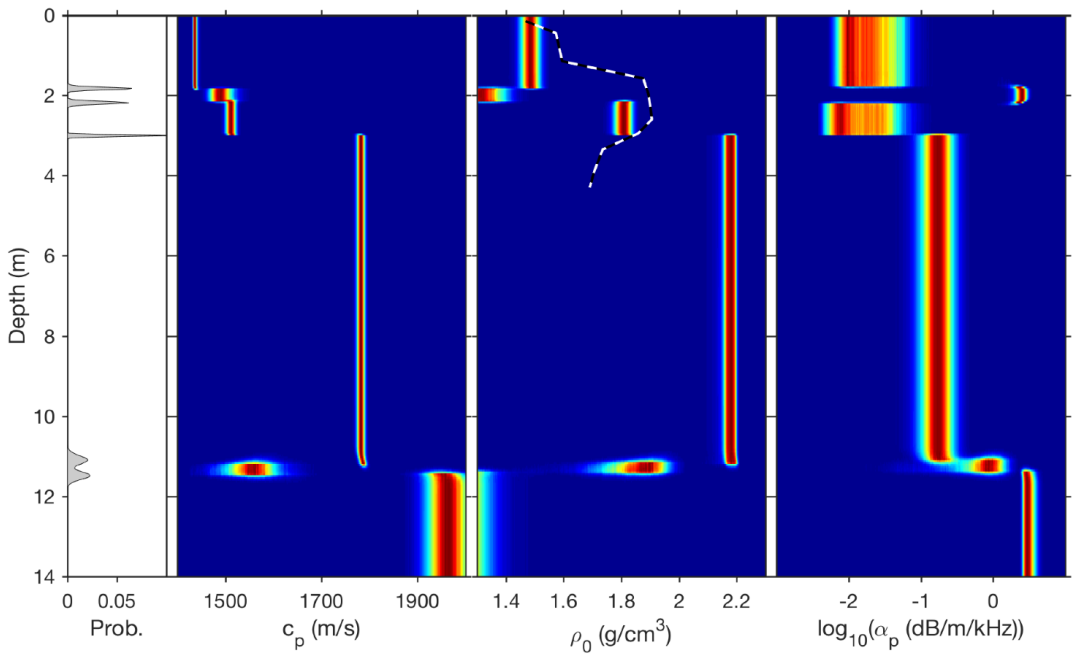

Figure 3.19: Marginal posterior probability profiles at 400 Hz for compressional velocity, density and log-attenuation as a function of depth in the sediment with a uniform bounded prior (only) on k at the PC52 site.

The inversion is based on parallel tempering rjMCMC sampling methods. The algorithm samples probabilistically over an unknown number of seabed interfaces and parameters of a zeroth- or first-order AR error model, with steps that include birth/death steps (adding/removing interfaces) and parameter perturbations. The parameters of new layers are proposed from uniform priors and fixed-D parameter perturbations are proposed in a PC parameter space. Parallel tempering is implemented to improve birth acceptance rates by running a series of interacting MCMC chains with successively relaxed (tempered) likelihoods. Data error covariance is addressed by a hierarchical AR error model. The total data residuals are examined *a posteriori* to confirm the general validity of the error model assumptions.

Model selection can be challenging in geoacoustic inverse problems. To control excessive and possibly unphysical structure in an initial trans-D inversion with wide bounds on the number of interfaces k, a second inversion was carried out with a more constrained upper bound, estimated using the BIC. At both sites, the trans-D inversion results obtained with the more constrained prior on k exhibited the same overall structure as obtained with the wider bounds but with less variability. The potentially unphysical layers at the SWAMI site were removed with the more constrained prior, but some dubious structure (particularly at depth) remained at the PC52 site.

The trans-D inversions of reflection coefficients suggest a thick ($\sim$9.5 m) and thin ($\sim$2 m) region of fine-grained/cohesive (muddy) sediments at the SWAMI and PC52 site, respectively, over a deeper region of coarse-grained (sandy) sediments. The trans-D inversion results agreed reasonably well with independent measurements, i.e., core measurements at both sites and chirp-seismic reflection horizons at the SWAMI site.

Chapter 4

Conclusion

Knowledge of geoacoustic properties of seabeds often represents the limiting factor in modelling shallow-water sound propagation. In particular, unconsolidated marine sediments have been little explored and are therefore less understood than harder coarse-grained sediments. Still, muddy seabeds are of interest to shallow-water acoustic research as they are commonly found. While direct measurements (e.g., coring) can be difficult, time consuming, and expensive, inferring geoacoustic properties from acoustic measurements is an economical alternative.

This thesis presented a Bayesian approach to inverting seabed reflection-coefficient data for geoacoustic properties of soft-layered seabeds at the New England Mud Patch, consistent with the objectives of the U.S. Office of Naval Research Seabed Characterization Experiment 2017 (SCBEX) to quantify uncertainties in seabed parameters estimated by geoacoustic inversion, and assess the resulting geoacoustic models and inversion methods [17].

The broadband wide-angle reflection-coefficient data were collected in late March, 2017, at the Shallow Water Acoustic Measurement Instrument (SWAMI) and Piston Core 52 (PC52) sites. The measurement geometry involved a broadband source towed near the surface of the water, and moored omni-directional receivers.

The first part of this thesis presented a linearized, ray-based Bayesian inversion of acoustic arrival-time data for high-precision estimation of experiment geometry and uncertainties, representing an important first step to inferring seabed properties using geoacoustic reflectivity inversion. Source-receiver ranges, source depths, receiver depths, and water depths at reflection points along the track were estimated to much higher precision than prior information based on GPS and bathymetry measurements. Grazing angles were computed using the high-precision experiment geometry with angle uncertainties computed using Monte Carlo methods. The experiment geome-

try uncertainties were obtained using analytic linearized estimates and verified with nonlinear analysis. The methods presented are general and can be used in other applications where accurate source and receiver locations and/or experiment geometry are required.

The second part applied nonlinear Bayesian geoaoustic inversion to the measured reflection-coefficient data. The trans-dimensional (trans-D) Bayesian formulation applied in this thesis is a general and powerful approach that rigorously estimated uncertainties by incorporating the geoacoustic model parametrization and data error model as unknowns in the problem. The trans-D posterior probability density (PPD) was sampled numerically by parallel tempering reversible jump Markov-chain Monte Carlo methods. The PPD provided parameter estimates with uncertainties quantified in terms of marginal posterior probability profiles for viscous grain-shearing (VGS) model parameters: porosity, grain-to-grain compressional modulus, material exponent, and compressional viscoelastic time constant. The VGS parameters were used to compute the geoacoustic properties of a fluid model of the sediment and dispersion within sediment layers. The porosity and density estimates at both sites compared well to core data for these parameters, and the interface depths at the SWAMI site agreed with reflection horizons estimated from two-way-travel-time data from a chirp-seismic survey. The assumption of Gaussian-distributed data residuals with correlations described by an autoregressive process were examined *a posteriori* to support parameter uncertainty estimates.

Two trans-D inversions with different priors on the number of interfaces k were applied at each site: one characterized by a Poisson distribution and wide bounds on k, and one with uniform bounds constrained to a smaller number of interfaces. The second inversion was carried out because the initial inversion results at each site appeared to include extraneous, potentially unphysical structure possibly due to theory errors caused by factors such as interface roughness and/or non-horizontal sediment layers. The more constrained upper bound on number of interfaces in the second inversion was based on the Bayesian information criterion (BIC) to provide an estimate of the number of interfaces resolved by the data. The more parsimonious model may be preferred in practice, although the BIC is only an approximate approach to model selection.

While the trans-D method estimates geoacoustic parameters for discrete homogenous layers in the sediment, the profiles obtained could be interpreted in terms of gradational transition regions of the mud-sand interface at both sites. The geoacoustic and porosity profiles at the SWAMI and PC52 sites pointed to a thick ($\sim$9.5 m)

and thin ($\sim$2 m) region, respectively, of fine-grained/cohesive (muddy) sediments over a deeper region of coarse-grained (sandy) sediments in agreement with independent knowledge of the seabed structure at each site.

References

[1] C. M. Ferla and F. B. Jensen, *Are Current Environmental Databases Adequate for Sonar Predictions in Shallow Water?* Springer, Dordrecht, 2002, pp. 555–562.

[2] F. B. Jensen, W. A. Kuperman, M. B. Porter, and H. Schmidt, *Computational Ocean Acoustics*, 2nd ed. New York, NY: Springer, 2011.

[3] E. L. Hamilton, "Geoacoustic modeling of the sea floor," *J. Acoust. Soc. Am.*, vol. 68, no. 5, pp. 1313–1340, November 1980.

[4] T. J. J. Hanebuth, H. Lantzsch, and J. Nizou, "Mud depocenters on continental shelves–appearance, initiation times, and growth dynamics," *Geo-Mar Lett*, vol. 35, no. 6, pp. 487–503, October 2015.

[5] B. Katsnelson, V. Petnikov, and J. Lynch, *Fundamentals of Shallow Water Acoustics*, ser. Underwater Acoustics. New York, NY: Springer, 2012.

[6] M. S. Ballard and K. M. Lee, "The acoustics of marine sediments," *Acoustics Today*, vol. 13, no. 3, pp. 11–18, Fall 2017.

[7] N. R. Chapman, "Modeling ocean-bottom reflection loss measurements with the plane-wave reflection coefficient," *J. Acoust. Soc. Am.*, vol. 73, no. 5, pp. 1601–1607, May 1983.

[8] D. E. Hannay and N. R. Chapman, "Inversion of geoacoustic profiles in thin-sediment environments from ocean bottom reflection loss data," in *Proceedings of OCEANS '93*. IEEE, 1993, pp. 381–386.

[9] S. E. Dosso and C. W. Holland, "Geoacoustic uncertainties from viscoelastic inversion of seabed reflection data," *IEEE JOE*, vol. 31, no. 3, pp. 657–671, July 2006.

[10] J. Dettmer, S. E. Dosso, and C. Holland, "Trans-dimensional uncertainty estimation for dispersive seabed sediments," *Geophysics*, vol. 78, no. 3, pp. WB63–WB76, May-June 2013.

[11] J. E. Quijano, S. E. Dosso, J. Dettmer, and C. Holland, "Fast computation of seabed spherical-wave reflection coefficients in geoacoustic inversion," *J. Acoust. Soc. Am.*, vol. 138, no. 4, pp. 2106–2117, October 2015.

[12] N. P. Chotiros, *Acoustics of the Seabed as a Poroelastic Medium*, ser. Springer briefs in oceanography. Springer and ASA Press, 2017.

[13] D. J. Battle, P. Gerstoft, W. S. Hodgkiss, W. A. Kuperman, and P. L. Nielsen, "Bayesian model selection applied to self-noise geoacoustic inversion," *J. Acoust. Soc. Am.*, vol. 116, no. 4, pp. 2043–2056, October 2004.

[14] J. Dettmer, S. E. Dosso, and C. Holland, "Model selection and Bayesian inference for high-resolution seabed reflection inversion," *J. Acoust. Soc. Am.*, vol. 125, no. 2, pp. 706–716, February 2009.

[15] J. Dettmer and S. E. Dosso, "Trans-dimensional matched-field geoacoustic inversion with hierarchical error models and interacting Markov chains," *J. Acoust. Soc. Am.*, vol. 132, no. 4, pp. 2239–2250, October 2012.

[16] S. E. Dosso, C. W. Holland, and M. Sambridge, "Parallel tempering for strongly nonlinear geoacoustic inversion," *J. Acoust. Soc. Am.*, vol. 132, no. 5, pp. 3030–3040, November 2012.

[17] D. P. Knobles and P. S. Wilson, "Seabed Characterization Experiment," accessed 2018-02-10. [Online]. Available: https://wwwext.arlut.utexas.edu/sbcex/

[18] D. C. Twichell, C. E. McClennen, and B. Butman, "Morphology and processes associated with the accumulation of the fine-grained sediment deposit on the southern New England shelf," *Journal of Sedimentary Petrology*, vol. 51, no. 1, pp. 269–280, March 1981.

[19] J. Goff, J. D. Chaytor, A. H. Reed, S. Liu, P. S. Wilson, and D. P. Knobles, "The coarse-to fine-grained boundary beneath the New England mud patch: Evidence from seismic and core data for an abrupt post-transgressive change in hydrologic regime on the continental shelf," *AGU Fall Meeting paper*, no. EP24B-01, 2016.

[20] K. M. Lee, M. S. Ballard, G. R. Venegas, P. S. Wilson, K. M. Dorgan, A. H. Reed, and E. Roosen, "Proc. Mtgs. Acoust. Preliminary characterization of surficial sediment acoustic properties and infauna in the New England Mud Patch," *J. Acoust. Soc. Am.*, vol. 26, no. 070003, 2017.

[21] C. W. Holland and J. Osler, "High-resolution geoacoustic inversion in shallow water: A joint time- and frequency-domain technique," *J. Acoust. Soc. Am.*, vol. 107, no. 3, pp. 1263–1279, March 2000.

[22] C. W. Holland, "Seabed reflection measurement uncertainty," *J. Acoust. Soc. Am.*, vol. 114, no. 4, pp. 1861–1873, October 2003.

[23] A. Tarantola, *Inverse Problem Theory and Methods for Model Parameter Estimation*, 2nd ed. Philadelphia, PA: Society for Industrial and Applied Mathematics, 2005.

[24] M. J. Buckingham, "Compressional and shear wave properties of marine sediments: Comparisons between theory and data," *J. Acoust. Soc. Am.*, vol. 117, no. 1, pp. 137–152, January 2005.

[25] ——, "On pore-fluid viscosity and the wave properties of saturated granular materials including marine sediments," *J. Acoust. Soc. Am.*, vol. 122, no. 3, pp. 1486–1501, September 2007.

[26] ——, "Response to "Comments on 'Pore fluid viscosity and the wave properties of saturated granular materials including marine sediments [J. Acoust. Soc. Am. 127, 2095–2098 (2010)]' "," *J. Acoust. Soc. Am.*, vol. 127, no. 4, pp. 2099–2102, April 2010.

[27] M. A. Biot, "Generalized theory of acoustic propagation in porous dissipative media," *J. Acoust. Soc. Am.*, vol. 34, no. 9, pp. 1254–1264, September 1964.

[28] C. W. Holland and J. Dettmer, "In situ sediment dispersion estimates in the presence of discrete layers and gradients," *J. Acoust. Soc. Am.*, vol. 133, no. 50, pp. 50–61, January 2013.

[29] J. Dettmer, S. E. Dosso, and C. W. Holland, "Full wave-field reflection coefficient inversion," *J. Acoust. Soc. Am.*, vol. 122, no. 6, pp. 3327–3337, December 2007.

[30] J. Dettmer, S. E. Dosso, and C. Holland, "Trans-dimensional geoacoustic inversion," *J. Acoust. Soc. Am.*, vol. 128, no. 6, pp. 3393–3405, December 2010.

[31] J. Dettmer, S. Molnar, G. Steininger, S. E. Dosso, and J. F. Cassidy, "Trans-dimensional inversion of microtremor array dispersion data with hierarchical autoregressive error models," *Geophys. J. Int.*, vol. 188, pp. 719–734, 2012.

[32] G. Steininger, J. Dettmer, S. E. Dosso, and C. W. Holland, "Trans-dimensional joint inversion of seabed scattering and reflection data," *J. Acoust. Soc. Am.*, vol. 133, no. 3, pp. 1347–1357, March 2013.

[33] P. J. Green, "Reversible jump Markov chain Monte Carlo computation and Bayesian model," *Biometrika*, vol. 82, no. 4, pp. 711–732, December 1995.

[34] ——, *Trans-dimensional Markov chain Monte Carlo*, ser. Oxford Statistical Science Series. Oxford: Oxford University Press, 2003, vol. 4, ch. 6, pp. 179–198.

[35] C. J. Geyer and J. Moller, "Simulation procedures and likelihood inference for spatial point processes," *Scandinavian Journal of Statistics*, vol. 21, no. 4, pp. 359–373, December 1994.

[36] A. Jasra, D. A. Stephens, and C. C. Holmes, "Population-based reversible jump Markov chain Monte Carlo," *Biometrika*, vol. 94, no. 4, pp. 787–807, December 2007.

[37] S. E. Dosso, J. Dettmer, G. Steininger, and C. W. Holland, "Efficient trans-dimensional Bayesian inversion for geoacoustic profile estimation," *Inverse Problems*, vol. 30, no. 11, pp. 1–29, October 2014.

[38] J. Belcourt, S. E. Dosso, C. W. Holland, and J. Dettmer, "Linearized Bayesian inversion for experiment geometry at the New England Mud Patch," forthcoming.

[39] J. Belcourt, C. W. Holland, S. E. Dosso, and J. Dettmer, "Trans-dimensional Bayesian geoacoustic inversion of spherical-wave reflection coefficients at the New England Mud Patch," forthcoming.

[40] C. W. Holland, "Coupled scattering and reflection measurements in shallow water," *IEEE JOE*, vol. 27, no. 3, pp. 454–470, July 2002.

[41] S. E. Dosso, M. R. Fallat, B. J. Sotirin, and J. L. Newton, "Array element localization for horizontal arrays via Occam's inversion," *J. Acoust. Soc. Am.*, vol. 104, no. 2, pp. 846–859, August 1998.

[42] S. E. Dosso and G. R. Ebbeson, "Array element localization accuracy and survey design," *Can. Acoust.*, vol. 34, no. 4, pp. 3–13, 2006.

[43] W. Telford, L. Geldart, and R. Sheriff, *Applied Geophysics*, 2nd ed. Cambridge, New York: Cambridge University Press, 1990.

[44] S. E. Dosso and M. J. Wilmut, "Bayesian acoustic source track prediction in an uncertain ocean environment," *IEEE JOE*, vol. 35, no. 4, pp. 811–820, October 2010.

[45] X. Ma, "Efficient inversion methods in underwater acoustics," Ph.D. dissertation, NJIT, Newark, NJ, May 2001.

[46] D. Thomson, S. E. Dosso, and D. R. Barclay, "Modeling AUV localization error in a long baseline acoustic positioning system," *IEEE Journal of Oceanic Engineering*, vol. PP, no. 9, pp. 1–14, December 2017.

[47] B. P. Rideout, S. E. Dosso, and D. E. Hannay, "Underwater passive acoustic localization of Pacific walruses in the northeastern Chukchi Sea," *J. Acoust. Soc. Am.*, vol. 134, no. 3, pp. 2534–2545, September 2013.

[48] E. K. Skarsoulis and S. E. Dosso, "Linearized two-hydrophone localization of a pulsed acoustic source in the presence of refraction: Theory and simulations," *J. Acoust. Soc. Am.*, vol. 138, no. 4, pp. 2221–2234, October 2015.

[49] M. D. Collins, W. A. Kuperman, , and H. Schmidt, "Nonlinear inversion for ocean-bottom properties," *J. Acoust. Soc. Am.*, vol. 92, no. 5, pp. 2770–2783, November 1992.

[50] A. Tolstoy, "Using matched-field processing to estimate shallow-water bottom properties from shot data taken in the Mediterranean Sea," *IEEE Journal of Oceanic Engineering*, vol. 21, no. 4, pp. 471–479, October 1996.

[51] Z.-H. Michalopoulou, "Matched-impulse-response processing for shallow-water localization and geoacoustic inversion," *J. Acoust. Soc. Am.*, vol. 108, no. 5, pp. 2082–2090, November 2000.

[52] M. S. Ballard, K. M. Becker, and J. A. Goff, "Geoacoustic inversion for the New Jersey Shelf: 3-D sediment model," *IEEE JOE*, vol. 35, no. 1, pp. 28–32, January 2010.

[53] J. Bonnel, S. E. Dosso, and N. R. Chapman, "Bayesian geoacoustic inversion of single hydrophone light bulb data using warping dispersion analysis," *J. Acoust. Soc. Am.*, vol. 134, no. 1, pp. 120–130, July 2013.

[54] C. W. Holland, P. L. Nielsen, J. Dettmer, and S. Dosso, "Resolving meso-scale seabed variability using reflection measurements from an autonomous underwater vehicle," *J. Acoust. Soc. Am.*, vol. 131, no. 2, pp. 1066–11 078, February 2012.

[55] D. G. T. Denison, C. C. Holmes, B. K. Mallick, and A. F. M. Smith, *Bayesian Methods for Nonlinear Classification and Regression.* New York, NY: Willey, 2002.

[56] W. H. Press, S. A. Teukolsky, W. T. Vetterling, and B. P. Flannery, *Numerical Recipes in FORTRAN*, 2nd ed. New York, NY: Cambridge University Press, 1992.

[57] S. Brooks, A. Gelman, G. L. Jones, and X.-L. Meng, *Handbook of Markov Chain Monte Carlo*, 1st ed., ser. CRC Handbooks of Modern Statistical Methods. Chapman and Hall /CRC, 2011.

[58] G. Steininger, "Determination of seabed acoustic scattering properties by trans-dimensional Bayesian inversion," Ph.D. dissertation, University of Victoria, Ottawa, 2013.

[59] J. Dettmer, S. E. Dosso, and C. Holland, "High performance computing methods for nonlinear Bayesian uncertainty quantification," *J. Acoust. Soc. Am*, vol. 143, no. 3, p. 1925, March 2018, program of the 175th Meeting of the Acoustical Society of America.

[60] J. D. Chaytor, *personal communication*, 16 July 2018, re: [EXTERNAL] SWAMI & PC52 Core Data.

[61] D. R. Jackson and M. D. Richardson, *High-Frequency Seafloor Acoustics.* Springer, 2007.

[62] J. Dettmer, "Geoacoustic reflectivity inversion: A Bayesian approach," Ph.D. dissertation, University of Victoria, Ottawa, 2006.

[63] S. E. Dosso and M. J. Wilmut, "Efficient Bayesian multi-source localization," *Canadian Acoustics*, vol. 40, no. 3, pp. 72–73, September 2012.

[64] D. Marion, A. Nur, H. Yin, and D. Han, "Compressional velocity and porosity in sand-clay mixtures," *Geophysics*, vol. 57, no. 4, pp. 554–563, April 1992.

[65] J. W. Tukey, "The future of data analysis," *Ann. Math. Statist.*, vol. 33, no. 1, pp. 1–67, 1962.